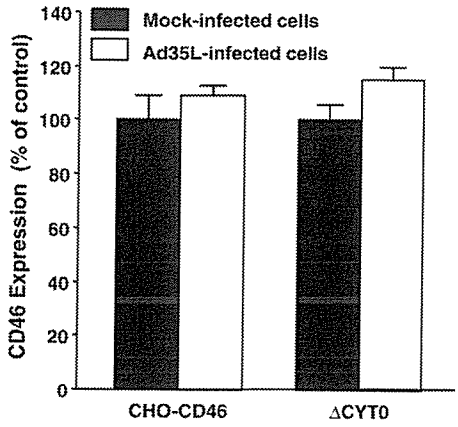

Fig. 8. CD46 expression levels in CHO transformants after infection with Ad35L. The CHO transformants expressing full-length CD46 or CD46ΔCYT0 were transduced with Ad35L at 3000 VP/cell for 1.5 h. After a 1.5-h incubation, the cells were subjected to flowcytometric analysis for measurement of CD46 expression. The data are expressed as the mean±S.D. (n=4).

CD46 downregulation might influence the infectivity of the viruses. Flowcytometric analysis demonstrated that CD46 downregulation did not occur in both CHO transformants expressing full-length CD46 or CD46ΔCYT0 following transduction with Ad35L (Fig. 8), suggesting that CD46 downregulation by Ad35 vectors was not involved in the increase in the transduction efficiencies of Ad35L in CHO cells expressing CD46ΔCYT0.

4. Discussion

Elucidation of the interaction between viruses and their receptors is of great importance for studies of virus pathogenicity. In addition, for the viruses that provide a framework for gene delivery vehicles, such information may help us not only to evaluate the transduction properties of virus vectors but also to improve virus vectors. In this study, CHO cells expressing CD46 deletion mutants and several monoclonal anti-CD46 antibodies were used to examine which regions are crucial for Ad35 infection. Infection experiments in cells expressing CD46 mutants lacking SCRs and blocking experiments using monoclonal anti-CD46 antibodies have already been used to determine the essential regions for infection of the pathogens recognizing CD46 in previous studies [16–18,29]. We applied this approach to elucidation of the crucial regions in CD46 for subgroup B Ad infection. The results presented herein demonstrated that the essential domains for Ad35 infection are located in SCR1 and 2, and that deletion of all the cytoplasmic domain in CD46 significantly increases Ad35 vector-mediated transduction.

Previous studies have demonstrated that MV binds to SCR1 and 2 [16,17], whereas infection of HHV6 is mediated by SCR2 and 3 [18]. Thus, SCR2 of CD46 is a crucial domain for all the human viruses utilizing CD46 (MV, HHV6, and subgroup B Ads). Moreover, SCR2-specific antibody M177 significantly inhibits the infection of all three viruses (Fig. 3) [18], suggesting that these viruses would interact with the region recognized by M177. The amino acids important for M177 binding, R69 and D70, which are located in the middle of SCR2 [30], are also present in CD46 of the cynomolgus monkey [31], which is susceptible to MV and HHV6. We also confirmed that primary cells isolated from the cynomolgus monkey were efficiently transduced with Ad35 vectors (data not shown).

Deletion of SCR1 as well as SCR2 largely decreased both the transduction efficiency and the cellular uptake of Ad35L (Figs. 3 and 4). However, SCR1-specific E4.3 and J4-48 did not significantly reduce the luciferase productions by Ad35L (Fig. 5). On the other hand, the antibody MEM-258, which also recognizes SCR1, significantly inhibited the Ad35 vector-mediated transduction and cellular uptake of Ad35L (Figs. 5 and 6). The amino acids important for binding of E4.3 and J4-48 are located on the top of SCR1 [31]. At present, it remains unclear where the epitope of MEM-258 is located within SCR1; however, the location of the epitope of MEM-258 would be different from those of E4.3 and J4-48, and would be important for Ad35 infection.

Recognition of SCR1 and 2 by Ad35 would be favorable for infection of Ad35. SCR1 and 2 are located on the upper region of CD46, leading to the decrease in electrostatic repulsion between the virus capsid and acidic cell surface proteins and the increase in attachment of Ad35 to the cell surface. Shayakhmetov and Lieber demonstrated that electrostatic repulsion between the virus capsid and cell surface is an important factor for Ad infection, especially for Ads possessing a short fiber shaft [32]. Ad35 has a shorter fiber shaft (9 nm) than Ad5 (37 nm).

During the preparation of this manuscript, two reports concerning the domains of human CD46 which interact with subgroup B Ads were published [25,33]. Gaggar et al. demonstrated that the subgroup B Ad-binding domain is located within SCR2 alone [33], while Fleischli et al. reported that the presence of both SCR1 and 2 is sufficient for infection of Ad35 and that binding of Ad35 is not confined to a single SCR domain [25]. Our data support the conclusion of Fleischli et al. The SCR2-specific antibody M177 and the deletion of SCR2 decreased Ad35 vector-mediated transduction (Figs. 3–6), suggesting that the region in SCR2 recognized by M177 would be important for interaction with Ad35. Luciferase production by Ad35L and cellular uptake of Ad35L in ΔSCR1 mutants was largely decreased, compared with CHO-CD46 cells (Figs. 3 and 4), suggesting that SCR1 would also play a role in Ad35 infection. Although the decrease in luciferase production and cellular uptake of Ad35L in the ΔSCR1 mutant might be due to conformational change of SCR2 by the deletion of SCR1, this is unlikely because the SCR2-specific antibody M177 showed positive staining in the ΔSCR1 mutant (Fig. 2). This suggests that the region recognized by M177 would hold an appropriate conformation in the ΔSCR1 mutant. Therefore, we conclude that both SCR1 and SCR2 are involved with Ad35 infection. The finding that the SCR1-specific antibody MEM-258 largely inhibited the transduction with Ad35L supports this conclusion (Figs. 5 and 6).

The cytoplasmic domain of human CD46 is not an absolute requirement in order for this protein to serve as an attachment receptor for Ad35 (Fig. 7). MV and HHV6 can also infect cells via mutant CD46 lacking the cytoplasmic domain [18,19]. However, the luciferase production was significantly increased in ΔCYT0, compared with that in CHO-CD46, in contrast, Ad35L mediated similar levels of luciferase productions in both CHO-CD46 and ΔCYT6. It remains unclear why the deletion of

the entire cytoplasmic domain of human CD46 increased the transduction efficiency, however, downregulation of CD46 was not observed in both CHO-CD46 and ΔCYT0 after transduction with Ad35L (Fig. 7). These results suggest that the increase in the transduction efficiencies of Ad35L in ΔCYT0 was not due to the lack of CD46 downregulation. One possibility for the increased transduction efficiencies in ΔCYT0 is that the amounts of CD46 which Ad35 vectors can access to would be increased by the deletion of the cytoplasmic domain. Maisner et al. demonstrated that CD46 are predominantly distributed in basolateral side of the cells and that CD46 lacking the entire cytoplasmic domain were transported to both apical and basolateral sides [34]. CD46ΔCYT0 might be more widely distributed than full-length CD46 in the CHO transformants, leading to the increase in the infection of Ad35 vectors. Another possibility is that the membrane-proximal 6 amino acids of the cytoplasmic domain in CD46 C2 isoform might contain a signal sequence for suppression of viral infection. Mouse macrophages expressing a tailless human CD46 mutant are more susceptible to MV infection than those expressing wild-type CD46 [35]. In addition to these functions of the cytoplasmic domain, the cytoplasmic domain plays important roles in immune responses through CD46, such as cytokine productions. Hirano et al. reported that the production of high levels of NO and IL-12 upon MV infection is dependent on the CD46 cytoplasmic domain [35]. Kurita-Taniguchi et al. demonstrated that intracellular phosphatase SHP-1 was found to be recruited to the cytoplasmic tail of human CD46 when human macrophages became sufficiently mature to produce IL-12 and NO in response to measles virus [36]. Therefore, the cytoplasmic domain might be involved with immune responses induced by Ad35 infection.

In summary, we demonstrated here that SCR1 and 2 of human CD46 are required for Ad35 infection, while the cytoplasmic domain of human CD46 is not crucial for an attachment receptor function for Ad35. These results offer insight into the interaction between human CD46 and subgroup B Ads, such as the internalization of Ad35 into the cells via CD46 and the crucial domain in the Ad35 fiber knob for binding to CD46.

Acknowledgements

We would like to thank Dr. Yasuko Mori (Laboratory of Virology and Vaccinology, National Institute of Biomedical Innovation, Osaka, Japan) for her advice on the cell culture. This work was supported in part by a Grants-in-Aid for Scientific Research from the Ministry of Education, Culture, Sports, Science, and Technology of Japan, and by grants for Health and Labour Sciences Research from the Ministry of Health, Labour, and Welfare of Japan.

References

[1] M.J. Havenga, A.A. Lemckert, O.J. Ophorst, M. van Meijer, W.T. Germeraad, J. Grimbergen, M.A. van Den Doel, R. Vogels, J. van Deutekom, A.A. Janson, J.D. de Bruijn, F. Uytdehaag, P.H. Quax, T. Logtenberg, M. Mehtali, A. Bout, Exploiting the natural diversity in adenovirus tropism for therapy and prevention of disease, J. Virol. 76 (2002) 4612–4620.

[2] J.C. De Jong, A.G. Wermenbol, M.W. Verweij-Uijterwaal, K.W. Slaterus, P. Wertheim-Van Dillen, G.J. Van Doornum, S.H. Khoo, J.C. Hierholzer, Adenoviruses from human immunodeficiency virus-infected individuals, including two strains that represent new candidate serotypes Ad50 and Ad51 of species B1 and D, respectively, J. Clin. Microbiol. 37 (1999) 3940–3945.

[3] R. Vogels, D. Zuijdgeest, R. van Rijnsoever, E. Hartkoorn, I. Damen, M.P. de Bethune, S. Kostense, G. Penders, N. Helmus, W. Koudstaal, M. Cecchini, A. Wetterwald, M. Sprangers, A. Lemckert, O. Ophorst, B. Koel, M. van Meerendonk, P. Quax, L. Panitti, J. Grimbergen, A. Bout, J. Goudsmit, M. Havenga, Replication-deficient human adenovirus type 35 vectors for gene transfer and vaccination: efficient human cell infection and bypass of preexisting adenovirus immunity, J. Virol. 77 (2003) 8263–8271.

[4] A. Gaggar, D.M. Shayakhmetov, A. Lieber, CD46 is a cellular receptor for group B adenoviruses, Nat. Med. 9 (2003) 1408–1412.

[5] A. Segerman, J.P. Atkinson, M. Marttila, V. Dennerquist, G. Wadell, N. Arnberg, Adenovirus type 11 uses CD46 as a cellular receptor, J. Virol. 77 (2003) 9183–9191.

[6] F. Sakurai, H. Mizuguchi, T. Hayakawa, Efficient gene transfer into human CD34+ cells by an adenovirus type 35 vector, Gene Ther. 10 (2003) 1041–1048.

[7] F. Sakurai, H. Mizuguchi, T. Yamaguchi, T. Hayakawa, Characterization of in vitro and in vivo gene transfer properties of adenovirus serotype 35 vector, Mol. Ther. 8 (2003) 813–821.

[8] T. Seya, J.R. Turner, J.P. Atkinson, Purification and characterization of a membrane protein (gp45-70) that is a cofactor for cleavage of C3b and C4b, J. Exp. Med. 163 (1986) 837–855.

[9] T. Seya, J.P. Atkinson, Functional properties of membrane cofactor protein of complement, Biochem. J. 264 (1989) 581–588.

[10] T. Seya, T. Hara, M. Matsumoto, Y. Sugita, H. Akedo, Complement-mediated tumor cell damage induced by antibodies against membrane cofactor protein (MCP, CD46), J. Exp. Med. 172 (1990) 1673–1680.

[11] D.M. Lublin, K.E. Coyne, Phospholipid-anchored and transmembrane versions of either decay-accelerating factor or membrane cofactor protein show equal efficiency in protection from complement-mediated cell damage, J. Exp. Med. 174 (1991) 35–44.

[12] F. Santoro, P.E. Kennedy, G. Locatelli, M.S. Malnati, E.A. Berger, P. Lusso, CD46 is a cellular receptor for human herpesvirus 6, Cell 99 (1999) 817–827.

[13] R.E. Dorig, A. Marcil, A. Chopra, C.D. Richardson, The human CD46 molecule is a receptor for measles virus (Edmonston strain), Cell 75 (1993) 295–305.

[14] H. Kallstrom, M.K. Liszewski, J.P. Atkinson, A.B. Jonsson, Membrane cofactor protein (MCP or CD46) is a cellular pilus receptor for pathogenic *Neisseria*, Mol. Microbiol. 25 (1997) 639–647.

[15] N. Okada, M.K. Liszewski, J.P. Atkinson, M. Caparon, Membrane cofactor protein (CD46) is a keratinocyte receptor for the M protein of the group A streptococcus, Proc. Natl. Acad. Sci. U. S. A. 92 (1995) 2489–2493.

[16] K. Iwata, T. Seya, Y. Yanagi, J.M. Pesando, P.M. Johnson, M. Okabe, S. Ueda, H. Ariga, S. Nagasawa, Diversity of sites for measles virus binding and for inactivation of complement C3b and C4b on membrane cofactor protein CD46, J. Biol. Chem. 270 (1995) 15148–15152.

[17] M. Manchester, A. Valsamakis, R. Kaufman, M.K. Liszewski, J. Alvarez, J.P. Atkinson, D.M. Lublin, M.B. Oldstone, Measles virus and C3 binding sites are distinct on membrane cofactor protein (CD46), Proc. Natl. Acad. Sci. U. S. A. 92 (1995) 2303–2307.

[18] H.L. Greenstone, F. Santoro, P. Lusso, E.A. Berger, Human herpesvirus 6 and measles virus employ distinct CD46 domains for receptor function, J. Biol. Chem. 277 (2002) 39112–39118.

[19] T. Seya, M. Kurita, K. Iwata, Y. Yanagi, K. Tanaka, K. Shida, M. Hatanaka, M. Matsumoto, S. Jun, A. Hirano, S. Ueda, S. Nagasawa, The CD46 transmembrane domain is required for efficient formation of measles-virus-mediated syncytium, Biochem. J. 322 (Pt 1) (1997) 135–144.

[20] T. Seya, T. Hara, M. Matsumoto, H. Akedo, Quantitative analysis of membrane cofactor protein (MCP) of complement. High expression of MCP on human leukemia cell lines, which is down-regulated during cell differentiation, J. Immunol. 145 (1990) 238–245.

[21] F. Sakurai, K. Kawabata, T. Yamaguchi, T. Hayakawa, H. Mizuguchi, Optimization of adenovirus serotype 35 vectors for efficient transduction in human hematopoietic progenitors: comparison of promoter activities, Gene Ther. 12 (2005) 1424–1433.

[22] H. Mizuguchi, N. Koizumi, T. Hosono, N. Utoguchi, Y. Watanabe, M.A. Kay, T. Hayakawa, A simplified system for constructing recombinant adenoviral vectors containing heterologous peptides in the HI loop of their fiber knob, Gene Ther. 8 (2001) 730–735.

[23] V. Krougliak, F.L. Graham, Development of cell lines capable of complementing E1, E4, and protein IX defective adenovirus type 5 mutants, Hum. Gene Ther. 6 (1995) 1575–1586.

[24] J.V. Maizel Jr., D.O. White, M.D. Scharff, The polypeptides of adenovirus. I. Evidence for multiple protein components in the virion and a comparison of types 2, 7A, and 12, Virology 36 (1968) 115–125.

[25] C. Fleischli, S. Verhaagh, M. Havenga, D. Sirena, W. Schaffner, R. Cattaneo, U.F. Greber, S. Hemmi, The distal short consensus repeats 1 and 2 of the membrane cofactor protein CD46 and their distance from the cell membrane determine productive entry of species B adenovirus serotype 35, J. Virol. 79 (2005) 10013–10022.

[26] M.K. Liszewski, I. Tedja, J.P. Atkinson, Membrane cofactor protein (CD46) of complement. Processing differences related to alternatively spliced cytoplasmic domains, J. Biol. Chem. 269 (1994) 10776–10779.

[27] G. Wang, M.K. Liszewski, A.C. Chan, J.P. Atkinson, Membrane cofactor protein (MCP; CD46): isoform-specific tyrosine phosphorylation, J. Immunol. 164 (2000) 1839–1846.

[28] A. Hirano, S. Yant, K. Iwata, J. Korte-Sarfaty, T. Seya, S. Nagasawa, T.C. Wong, Human cell receptor CD46 is down regulated through recognition of a membrane-proximal region of the cytoplasmic domain in persistent measles virus infection, J. Virol. 70 (1996) 6929–6936.

[29] Y. Mori, T. Seya, H.L. Huang, P. Akkapaiboon, P. Dhepakson, K. Yamanishi, Human herpesvirus 6 variant A but not variant B induces fusion from without in a variety of human cells through a human herpesvirus 6 entry receptor, CD46, J. Virol. 76 (2002) 6750–6761.

[30] C.J. Buchholz, D. Koller, P. Devaux, C. Mumenthaler, J. Schneider-Schaulies, W. Braun, D. Gerlier, R. Cattaneo, Mapping of the primary binding site of measles virus to its receptor CD46, J. Biol. Chem. 272 (1997) 22072–22079.

[31] E.C. Hsu, S. Sabatinos, F.J. Hoedemaeker, D.R. Rose, C.D. Richardson, Use of site-specific mutagenesis and monoclonal antibodies to map regions of CD46 that interact with measles virus H protein, Virology 258 (1999) 314–326.

[32] D.M. Shayakhmetov, A. Lieber, Dependence of adenovirus infectivity on length of the fiber shaft domain, J. Virol. 74 (2000) 10274–10286.

[33] A. Gaggar, D.M. Shayakhmetov, M.K. Liszewski, J.P. Atkinson, A. Lieber, Localization of regions in CD46 that interact with adenovirus, J. Virol. 79 (2005) 7503–7513.

[34] A. Maisner, M.K. Liszewski, J.P. Atkinson, R. Schwartz-Albiez, G. Herrler, Two different cytoplasmic tails direct isoforms of the membrane cofactor protein (CD46) to the basolateral surface of Madin–Darby canine kidney cells, J. Biol. Chem. 271 (1996) 18853–18858.

[35] A. Hirano, Z. Yang, Y. Katayama, J. Korte-Sarfaty, T.C. Wong, Human CD46 enhances nitric oxide production in mouse macrophages in response to measles virus infection in the presence of gamma interferon: dependence on the CD46 cytoplasmic domains, J. Virol. 73 (1999) 4776–4785.

[36] M. Kurita-Taniguchi, A. Fukui, K. Hazeki, A. Hirano, S. Tsuji, M. Matsumoto, M. Watanabe, S. Ueda, T. Seya, Functional modulation of human macrophages through CD46 (measles virus receptor): production of IL-12 p40 and nitric oxide in association with recruitment of protein-tyrosine phosphatase SHP-1 to CD46, J. Immunol. 165 (2000) 5143–5152.

Available online at www.sciencedirect.com
ScienceDirect
ELSEVIER
Biochemical and Biophysical Research Communications 349 (2006) 1372–1377
BBRC
www.elsevier.com/locate/ybbrc

Regulation of IL-27p28 gene by lipopolysaccharide in dendritic DC2.4 cells ☆

Maki Kamakura [a], Keiko Morisawa [a], Hideyuki Komi [a], Ayako Tomatani [a], Fumiji Saito [a], Yuko Konishi [a], Ya Jin [b], Takashi Manabe [b], Masayuki Kuroda [c], Shosuke Imai [c], Hiroyuki Mizuguchi [d], Taketoshi Taniguchi [a,*]

[a] *Laboratory of Molecular Biology, Medical Research Center, Kochi Medical School, Kochi, Japan*
[b] *Department of Chemistry, Faculty of Science, Ehime University, Matsuyama, Japan*
[c] *Department of Molecular Microbiology and Infections, Kochi Medical School, Kochi, Japan*
[d] *National Institute of Biomedical Innovation, Osaka, Japan*

Received 28 August 2006
Available online 12 September 2006

Abstract

To elucidate the regulation of IL-27p28 gene, we analyzed the promoter region of the gene in DC2.4 cells with or without lipopolysaccharide (LPS)-treatment. The results indicate that a region (−648 to −364) of p28 promoter was responsible for LPS-induction. EMSA with DNA probes within the region reveals that binding of GATA motif bound proteins was decreased by LPS-treatment. We identified one of the proteins as non-POU domain-containing octamer binding protein (NonO). Taken together, LPS-induced activation of IL-27p28 gene can be accounted for by the displacement of bound NonO protein from the IL-27p28 promoter.

Keywords: Th1/Th2 cells; Cytokine; Dendritic cells; Gene regulation; Reporter assay

The differentiation of naive $CD4^+$ T (Th0) cells into Th1 or Th2 cells is a critical process in the development of immune responses. Th1 cells promote cellular immunity, while Th2 cells promote humoral immunity. The development of Th1 and Th2 cells from Th0 cells is molded by environmental and genetic factors that act at the level of antigen presentation [1,2]. The cytokines that are subsequently produced by the APC play crucial roles in the polarization of Th cells. IL-27 appears to be produced early by activated APC. It is essential for early initiation of Th1 responses but it is not necessary for the maintenance of Th1 response [3–5] because mRNA expression of the IL-27 receptor, TCCR [6] or WSX-1 [5] was high on Th0 cells but low on differentiated Th1 and Th2 cells [6]. As for IL-12 receptors, IL-12Rβ1 is expressed on Th0 cells but IL-12Rβ2 is not. IL-12Rβ2 is induced by the action of IL-27 on Th0 cells, enables IL-12 to activate Th1 cells, and functions for the maintenance of Th1 response [7,8].

We used unique rat strains, Lewis (LEW) and Brown Norway (BN) rats, which are entirely different with regard to their tendency to generate particular Th immune responses (Th1 and Th2, respectively), and their susceptibility to experimentally induced autoimmune diseases [9]. We demonstrated that treatment with heat-killed *Mycobacterium tuberculosis* (*M. tb*) upregulated the expression of the IL-27p28 and EBI3 genes in naive LEW rat splenocytes but had no effect on the expression of these genes in naive BN rat splenocytes and among them dendritic cells produced IL-27 [10]. Rissoan et al. have reported that human myeloid DCs (designated DC1) produce large amounts of IL-12 after CD40L activation and induce Th0 cells to differentiate into Th1 cells, in contrast, plasmacytoid DCs (designated DC2) induce Th0 cells to differentiate into

☆ This work was supported by a grant to T.T. from the president research fund of Kochi University.
* Corresponding author. Fax: +81 88 880 2431.
E-mail address: taniguch@kochi-u.ac.jp (T. Taniguchi).

0006-291X/$ - see front matter © 2006 Published by Elsevier Inc.
doi:10.1016/j.bbrc.2006.09.004

Th2 cells [11]. We observed that most of the LEW rat DCs have the typical characteristics of DC1, while most of the BN rat DCs appear to be DC2-type cells and DC1 seems to be capable to produce IL-27 in an innate immune response. Here we report the regulation mechanism of IL-27p28 gene in mouse bone marrow-derived dendritic DC2.4 cells by the treatment with LPS and suggest that a factor, non-POU domain-containing octamer binding protein (NonO), seems to play a critical role for LPS-induced regulation of IL-27p28 and initial polarization of naive Th cells.

Materials and methods

Cell culture and treatment with stimulators. The immortalized murine DC lines, DC2.4(H-2b) were provided by Dr. K.L. Rock (Department of Pathology, University of Massachusetts Medical School, Worcester, MA) [12] and Dr. N. Okada (Department of Biopharmaceutics, Kyoto Pharmaceutical University, Kyoto) [13]. The DC2.4 cells were cultured in complete RPMI1640 medium supplemented with 2 mM L-glutamine, 100 μg/ml streptomycin, and 100 U/ml penicillin, 100 μM non-essential amino acid, and 50 μM 2-mercaptoethanol (2-ME), and 5% calf serum CS. Cells were plated at a density of 1×10^6 cells/ml and treated with or without 100 ng/ml LPS (from *Escherichia coli* 055:B5, Sigma), 5×10^6 cells/ml *E. coli* (HB101), or 10 μg/ml *M. tb* prepared from *M. tuberculosis* strain H37Ra (Difco) as described previously [10] for 6 h.

RT-PCR. RT-PCR was performed as previously reported [14]. The PCR product quantities were normalized relative to hypoxanthine phosphoribosyltransferase (HPRT) amounts. IL-27p28: sense, 5′-ATCTCCCC AATGTTTCCCTGACCT; antisense, 5′-GGCTCTTGGGGAGGTAG TTGAG (amplified fragment of 159 bp). HPRT: sense, 5′-GTGG CCCTCTGTGTGCTGAA; antisense, 5′-TTATGTCCCCCGTTGACTG GTC (amplified fragment of 157 bp).

Construction of adeno-reporter vectors and preparation of recombinant adeno-reporter viruses. We deduced a DNA sequence of a rat IL-27p28 promoter by searching for homology in databases of rat genome DNA using a murine IL-27p28 (Accession Nos. AY099297, NM145636) sequence as a probe. We prepared three forward primers (−1037-sense, GCTAGCCTAAAAGGATCGCTGTGGTC; −648-sense, GCTAGCTG ACCCCCTAATCCTATGTG; −364-sense, GCTAGCCTGGCCATCT GTCATTCAC) and one reverse primer (AGATCTGTGTGCAGCCA TCTCCTG). We produced DNAs of rat IL-27p28 promoter by PCR with the above primers using a DNA from spleen cells of LEW rat as a template. The rat IL-27p28-promoter DNAs were ligated with a pGV-B2 vector (Toyo Inc. Co. Ltd, Tokyo, Japan) at *Nhe*I and *Bgl* II sites individually. These plasmids were digested with *Nhe*I and *Not*I, and DNA fragments of IL-27p28-promoter and luciferase unit were ligated with an adeno-shuttle plasmid, pHM5 [15], and then the reporter units were transferred into a fiber-modified adenovirus vector, AdHM15-RGD [13]. The adenovirus was propagated in 293 cells, purified by two rounds of sucrose density gradient centrifugation, and stored at −80 °C. Titer of adenovirus particles was determined by the method of Karber's method [16].

Viral transduction and luciferase assay. A serum free medium (500 μl) containing 1×10^5 DC2.4 cells was incubated in each well of a 12-well plate for 4 h, removed medium and viral reporter gene particles (MOI 10) were added. After 2 h, 500 μl of culture medium was added to each well and after 24 h of culture, LPS was added. The cells were cultured in the presence or absence of 100 ng/ml LPS for 24 h. The cells were harvested, washed, and disrupted in 50 μl of Lysis buffer (Promega) by sonication. Luciferase activity was assayed with Luciferase Assay System E1500 (Promega).

Preparation of nuclear extracts and electrophoretic mobility shift assay (EMSA). Nuclear extracts were prepared as reported previously [17]. Protein concentrations were determined by the Bradford method [18]. EMSA was performed as described previously [17]. The sequences of the sense and antisense strands of double-stranded oligonucleotides used as probes in EMSA were as follows: ΔE-sense, 5′-TTACAGACAC CTGAATG; ΔE-anti-sense, 5′-CCTAGACTAAGCCTTC; GATA-sense, 5′-CTTCAGCCATCTGGTAAACC; GATA-antisense, 5′-GGTTTAC CAGATGGCTGAAG; NFκB-sense, 5′- TCTTATGGGTATTCCCTTA; NFκB-antisense, 5′-TAAGGGAATTACCCATAAGA. These sequences were identical in rat and mouse IL-27p28 promoter. Cold GATA competitor was used as the same GATA DNA probe and mutated GATA competitor was as follows; mutGATA-sense, 5′-CTTCAGCC**TAG**TGG TAAACC; mutGATA-antisense, 5′-GGTTTACCA**CTA**GGCTGAAG.

For protection assay, nuclear extracts (2 μg) were preincubated with 1 (lane 2), 2 μg (lane 3) of anti-NonO/p54nrb IgG (Santa Cruz Biotechnology, Inc.), or 2 μg of normal IgG (lane 4) for 30 min on ice, followed by the addition of the ^{32}P-labeled double-stranded GATA DNA fragment and EMSA was performed.

Construction of a mutated GATA-like motif reporter plasmid and luciferase assay. A mutated GATA-like motif reporter plasmid was constructed by two-step PCR. First PCR was performed with either mutGATA-sense and Luc-antisense (GTTTTTGGCGTCTTCCAT) primers or mutGATA-antisense and pGV-B2-sense (CTAGCAAAATAGGCTG TCCCC) primers using the wild type pGV-B2-IL-27p28 promoter (−648) as a template. Both PCR products were denatured, annealed, and then second PCR was performed with pGV-B2-sense and Luc-antisense primers. The PCR product was directly digested with *Nhe*I and *Bgl*II, and then ligated with a pGV-B2 vector at *Nhe*I and *Bgl*II sites.

The reporter constructs of wild type or mutated GATA-like motif were transfected with DC2.4 cells using FuGENE HD (Roche) according to the manufacturer's manual. A mixture of 5 μg pGV-B2-p28/luciferase with wild type or mutated GATA motif, 1.25 μg *Renilla* luciferase (RL)-CMV, 15 μl FuGENE HD, and 250 μl H_2O was added into 7.5×10^5 DC2.4 cells cultured in 3 ml of RPMI1640/4% calf serum in a 60 mm dish. Six hours after transfection, the cells were treated with 100 ng/ml LPS for 24 h. The luciferase activity was measured with the Dual luciferase Reporter System (Promega). The firefly luciferase activity was normalized against *Renilla* luciferase activity of the same sample.

Preparation of GATA motif binding proteins and identification of a GATA motif bound protein. A synthetic biotin-labeled GATA DNA as described above was preliminarily incubated with 2 mg of streptavidin–magnetic beads (Roche Molecular Systems, Inc.) and then incubated with 250 μg DC2.4 nuclear proteins treated with or without LPS on a rotator at 4 °C for 1 h. DNA-bound proteins were washed with 500 μl of 75 mM KCl/Binding buffer (20 mM Tris–HCl, pH 8.0, 1 mM EDTA, 15% glycerol, and 0.05% NP-40) three times and then eluted with 50 μl of 1 M KCl/Binding buffer twice. The proteins in the eluate were precipitated by adding the equal volumes of 20% TCA and centrifugation, and dissolved in Destreak rehydration buffer. Affinity-purified proteins from DC2.4 nuclear extracts were subjected to two-dimensional electrophoresis (2-DE) with IPGphore isoelectric focusing (IEF) (pH3 to10 or pH6 to11) (Amersham Biosciences) and SDS–PAGE. The gel was stained with either CBB staining kit (Invitrogen) or silver staining kit (Amersham Biosciences). The corresponding band was excised from the gel and then incubated at 37 °C in 10 μl of 10 ng/μl trypsin (Promega) /50 mM ammonium bicarbonate for 16 h. The masses of the trypsin-digested peptides were determined by matrix-assisted laser desorption/ionization time-of-flight mass spectroscopy (MALDI-TOF-MS) using a Voyager DE-PRO instrument (Perseptive Biosystems, Framingham, MA). Protein identification was achieved by mass fingerprinting using the Mascot database created by Matrix Science (London, United Kingdom).

Results

Stimulation of IL-27p28 by treating DC2.4 cells with stimulators

We have previously observed that when LEW rat splenocytes were treated with *M. tb*, the expression of the

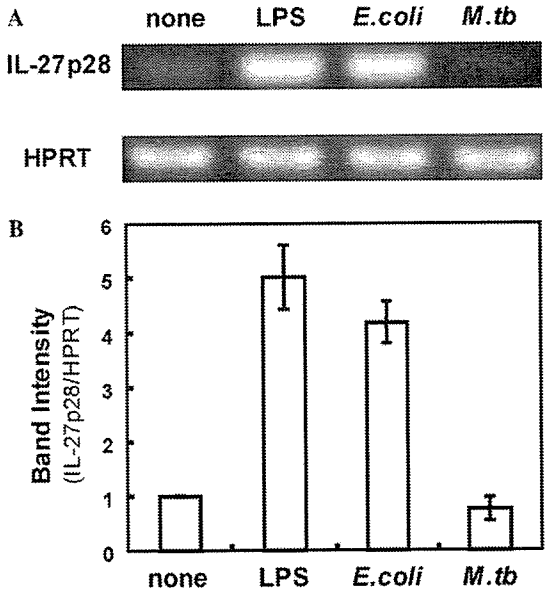

Fig. 1. Effect of stimuli on IL-27p28 expression in DC2.4 cells. (A) DC2.4 cells were cultured with 100 ng/ml LPS, 5×10^6 cells/ml alive *E. coli*, and 10 μg/ml *M. tb* for 6 h, total RNA was extracted, and IL-27p28 mRNA was measured by RT-PCR as described in Materials and methods. PCR products were separated on an agarose gel and stained with ethidium bromide. (B) The IL-27p28 bands were quantified by densitometry. Densitometric ratio of IL-27p28/HPRT mRNA is shown. Three independent experiments were performed and results are expressed as means ± SEM.

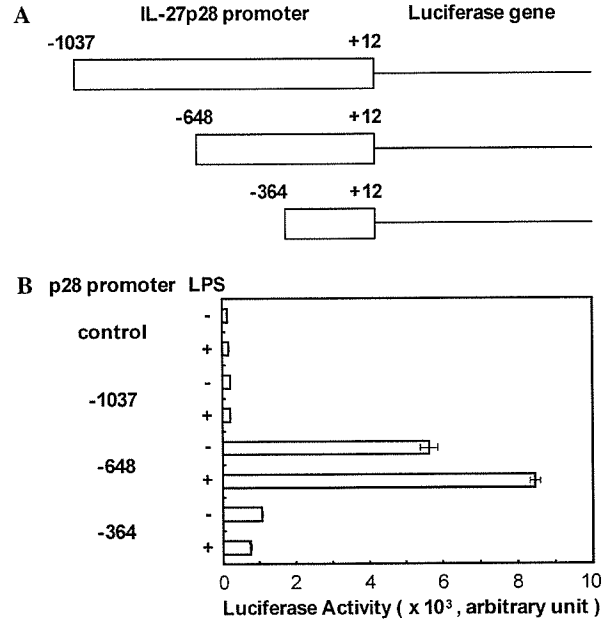

Fig. 2. Effect of LPS-treatment on IL27p28 promoter-derived luciferase activities (A) Schematic representation of the IL-27p28 promoter constructs used. (B) DC2.4 cells were infected with Ad-RGD-IL27p28 promoter-reporter virus (MOI 10) for 24 h and then stimulated with 100 ng /ml LPS for 24 h. Luciferase activity was measured as described in Materials and methods. The results are shown as means ± SEM.

IL-27p28 gene was increased with *M. tb* in a dose-dependent manner. Immunohistochemical analysis reveals that dendritic-like cells produce IL-27. We derived dendritic cells from bone marrows of naive LEW rats by incubating the cells with mouse GM-CSF. LEW rat BMDCs produced IL-27p28 mRNA in the absence of *M. tb* treatment and this expression is not affected by *M. tb* treatment [10]. No response to *M. tb* on the IL-27 expression in BMDCs was due to lack of TLR9 in BMDCs. However, TLR4 was detectable and IL-27p28 gene was stimulated by treating the BMDCs with LPS. We obtained an established mouse BMDC line, DC2.4 cells, and the expression of the IL-27p28 gene was examined by RT-PCR after treating DC2.4 cells with LPS, alive *E. coli*, and *M. tb*. as described in Materials and methods (Fig. 1A and B). As we expected, *M. tb* did not stimulate the expression of IL-27p28 gene but both LPS and *E. coli* stimulated IL-27p28 expression 5-fold and 4.2-fold, respectively. The latter observation was coincident with previous report of Schnurr et al. [19].

LPS-Regulatory region of IL-27p28 promoter

To elucidate the mechanism for LPS-dependent induction of IL-27p28 gene, we constructed three depleted IL-27p28 promoter-driven reporter genes as described in Materials and methods (Fig. 2A). The IL-27p28 promoter (−1037, −648, −364)/luciferase adeno-virus was infected with DC2.4 cells and luciferase activity was measured (Fig. 2B). The luciferase activity of −1037 promoter was low regardless of LPS-treatment, whereas −648 promoter-derived luciferase was enhanced by the treatment of LPS. The reporter gene with −364 promoter was still active but we did not observe any significant effect of LPS-treatment. Thus, LPS-responsive element seems to be located between −648 and −364 IL-27p28 promoter region.

Analyses of a binding protein(s) for LPS-responsive element of IL-27p28 promoter

To investigate what factor interacts with the LPS-responsive element and the regulation of the IL-27p28 gene, we first searched the sequence between −648 and −364 of the promoter with TFSEARCH: Searching Transcription Factor Binding Sites (ver 1.3) (http://www.cbrc.jp/research/db/TFSEARCH.html) and deduced some predicted transcription factor binding sequences within the region as shown in Fig. 3A. We produced synthetic double-stranded DNA probes and 5′-end ^{32}P-labeled DNAs were used as probes as described in Materials and methods. 5′-end ^{32}P-labeled single-strand nucleotides were also used as a primer as shown in Fig. 3A to produce longer double-strand DNA by PCR. EMSA was performed by incubating a DNA probe and nuclear extracts of DC2.4 cells treated with or without LPS (Fig. 3B). Fig. 3B shows that binding of a GATA motif binging protein(s) was decreased by the treatment with LPS, while ΔE and NFκB sequence binding protein(s) were not significantly affected by the LPS-treatment. The GATA motif bound protein(s)

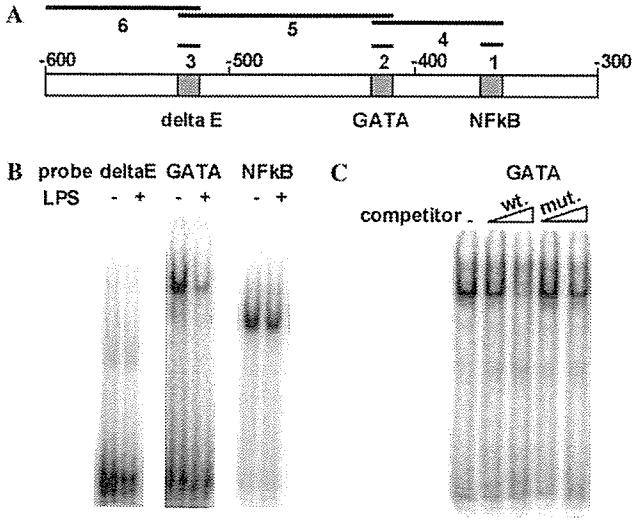

Fig. 3. Analysis of binding proteins on IL-27p28 promoter (−648 to −364). (A) Predicted transcriptional factor binding sequence motifs. (B) EMSA experiments were performed using nuclear extracts from DC2.4 cells cultured in the absence or presence of LPS as described in Materials and methods. The ΔE, GATA, or NFκB motif binding pattern are shown. (C) The GATA binding protein was disrupted with cold wild type GATA DNA (10-, or 100-fold excess) but not with mutated GATA DNA (10-, or 100-fold excess).

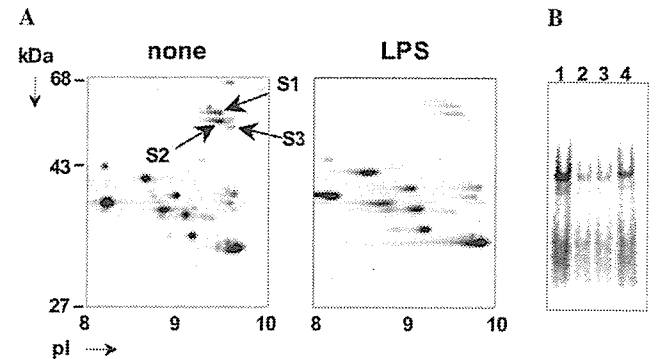

Fig. 5. LPS-dependent changes in GATA motif binding proteins of DC2.4 nuclear extracts and identification of a GATA motif bound protein(s). (A) GATA motif binding proteins were purified by GATA DNA affinity from nuclear extracts of DC2.4 cells cultured in the absence or presence of LPS and analyzed by 2-DE. Spots (S1, S2, and S3) corresponding to the LPS-dependent changes on 2-DE gel were analyzed by mass fingerprinting as described in Materials and methods. (B) The GATA motif bound protein was confirmed with anti-NonO antibody. Nuclear proteins (2 μg) were preincubated at 0 °C with anti-NonO antibody (lanes 2, and 3), normal IgG (lane 4) or without any antibody (lane 1) for 30 min before addition of the labeled GATA DNA probe and then EMSA was performed.

was diminished by the addition of cold GATA DNA competitor but not with mutated GATA DNA (Fig. 3C). This indicates that the bound protein(s) recognizes the GATA motif sequence.

To confirm that the GATA-like motif is an essential *cis*-element for LPS-induction of IL-27p28 gene, we constructed a reporter gene in which the GATA-like motif was mutated as mentioned in Materials and methods. The IL-27p28 promoter (−648)/luciferase reporter plasmid or a mutated GATA-like motif reporter plasmid was transfected with DC2.4 cells and luciferase activity was measured (Fig. 4). The luciferase activity of the wild type reporter gene was increased by the treatment with LPS, whereas the activity of mutated GATA-like motif reporter gene was increased without LPS-treatment and LPS-treatment further increased the activity slightly (Fig. 5).

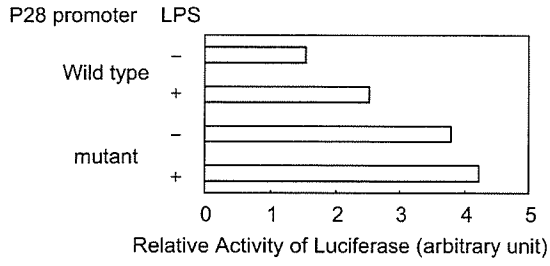

Fig. 4. The GATA-like motif is a cis-element for LPS-induction of IL-27p28 gene. The IL-27p28 promoter (−648)/luciferase reporter plasmid or a mutated GATA-like motif reporter plasmid was transfected with DC2.4 cells. Six hours after transfection, the cells were treated with 100 ng/ml LPS for 24 h and then luciferase activity was measured. The firefly luciferase activity was normalized against *Renilla* luciferase activity of the same sample. Three independent experiments were performed and the same results were obtained. One of the results is shown.

A GATA motif binding protein(s) was isolated by GATA DNA-affinity and separated with 2-DE and LPS-induced changes in protein spots were detected (Fig. 4A). The corresponding spots were pinched off, digested with trypsin, and analyzed with MALDI-TOF mass spectroscopy. The spot S1, S2 proteins were both identified as non-POU domain-containing octamer binding protein (NonO) by mass fingerprinting using the Mascot database and the spot S3 was identified as polypyrimidine tract binding protein (PTB). Difference in migration in terms of pI and mass for S1 and S2 seems to be post-modification of NonO.

Confirmation of the GATA motif bound protein as NonO

We performed supershift assay with anti-NonO antibody. The EMSA band with GATA DNA probe was not shifted but diminished with anti-NonO antibody (Fig. 4B lanes 2 and 3). This indicates that the factor bound to GATA motif in IL-27p28 promoter was NonO, which was displaced by the LPS treatment, resulting in activation of IL-27p28 gene.

Discussion

The first event in an innate immune response in mammals is the activation of macrophage and DCs, which engulf invading pathogens and secrete cytokines that activate other aspects of the immune response. To address the activation mechanism of IL-27 in DCs, we used mouse DC cell line DC2.4 cells and induced IL-27 by LPS-treatment. In this study we found that a repressive factor(s) interacted in GATA-like sequence of IL-27p28 promoter and LPS-treatment removed the factor(s), resulting in

activation of IL-27 gene. The factors were identified as NonO and PTB. In general LPS is transferred to the transmembrane signaling receptor, toll-like receptor 4 (TLR4), and MD-2, and stimulates the activation of various MAPK pathways, the IKK pathway, and the PI3K-Akt pathway. These pathways directly or indirectly phosphorylate and activate or inactivate various transcription factors [20]. The nonO gene was expressed routinely high in DC2.4 cells and LPS-treatment did not affect the expression (data not shown). Thus, we speculate that nonO seems to be phosphorylated by LPS-treatment and displaced from the promoter in DC2.4 cells. Our preliminary result indicates that the expression of IL-27p28 gene was enhanced when siRNA for nonO was transfected and suppressed the nonO expression (personal communication, Keiko Morisawa et al.).

Similar phenomenon was observed in IL-12p40 promoter [21]. In stimulated human monocytes the binding of NFκB, p50/65, C/EBPβ, and PU.1 to the IL-12p40 promoter was detected, while a binding of GATA sequence binding protein (GAP-12) was observed in resting cells, thereby repressing inducible IL-12p40 transcription in monocytes. This phenomenon was similar to the present study of the IL-27p28 promoter. Although GATA sequence in sense strand of IL-12p40 promoter and GATG sequence in antisense strand of IL-27p28 promoter are different, whether the same factors interact in these promoter is still to be elucidated.

We identified the GATA motif binding factors as NonO and PTB. NonO (mouse) and p54nrb (human) are highly homologous to the C-terminal of PTB-associated splicing factor (PSF) and forms a DNA-binding heterodimer which are shown to repress basal transcription of the human CYP17 gene involved in steroidogenesis and PSF in this complex interacts directly with the repressor Sin3A which in turn recruits a class I histone deacetylase (HDAC), a known partner of Sin3A in the mediation of transcriptional repression. This repression is alleviated by cAMP stimulation, phosphatase activity, and increased binding of SF-1/PSF/p54nrb to the promoter, together with the release of Sin3A-HDAC from the complex [22–24]. Taken together, NonO and related proteins interact with the IL-27 promoter in resting stage and by LPS stimulation the complex is displaced from the promoter and activates the IL-27 gene.

Acknowledgment

We thank Dr. M. Rashel for helping with manuscript preparation.

Appendix A. Supplementary data

Supplementary data associated with this article can be found, in the online version, at doi:10.1016/j.bbrc.2006.09.004.

References

[1] C.S. Hsieh, S.E. Macatonia, A. O'Garra, K.M. Murphy, T cell genetic background determines default T helper phenotype development in vitro, J. Exp. Med. 181 (1995) 713–721.
[2] M.L. Guler, J.D. Gorham, C.S. Hsieh, A.J. Mackey, R.G. Steen, W.F. Dietrich, K.M. Murphy, Genetic susceptibility to Leishmania: IL-12 responsiveness in TH1 cell development, Science 271 (1996) 984–987.
[3] A.Y. Park, B.D. Hondowicz, P. Scott, IL-12 is required to maintain a Th1 response during Leishmania major infection, J. Immunol. 165 (2000) 896–902.
[4] G. Yap, M. Pesin, A. Sher, Cutting edge: IL-12 is required for the maintenance of IFN-gamma production in T cells mediating chronic resistance to the intracellular pathogen, *Toxoplasma gondii*, J. Immunol. 165 (2000) 628–631.
[5] H. Yoshida, S. Hamano, G. Senaldi, T. Covey, R. Faggioni, S. Mu, M. Xia, A.C. Wakeham, H. Nishina, J. Potter, C.J. Saris, T.W. Mak, WSX-1 is required for the initiation of Th1 responses and resistance to L. major infection, Immunity 15 (2001) 569–578.
[6] Q. Chen, N. Ghilardi, H. Wang, T. Baker, M.H. Xie, A. Gurney, I.S. Grewal, F.J. de Sauvage, Development of Th1-type immune responses requires the type I cytokine receptor TCCR, Nature 407 (2000) 916–920.
[7] S.J. Szabo, A.S. Dighe, U. Gubler, K.M. Murphy, Regulation of the interleukin (IL)-12R beta 2 subunit expression in developing T helper 1 (Th1) and Th2 cells, J. Exp. Med. 185 (1997) 817–824.
[8] F. Brombacher, R.A. Kastelein, G. Alber, Novel IL-12 family members shed light on the orchestration of Th1 responses, Trends Immunol. 24 (2003) 207–212.
[9] G.J. Fournie, B. Cautain, E. Xystrakis, J. Damoiseaux, M. Mas, D. Lagrange, I. Bernard, J.F. Subra, L. Pelletier, P. Druet, A. Saoudi, Cellular and genetic factors involved in the difference between Brown Norway and Lewis rats to develop respectively type-2 and type-1 immune-mediated diseases, Immunol. Rev. 184 (2001) 145–160.
[10] F. Saito, Y. Ohno, K. Morisawa, M. Kamakura, A. Fukushima, T. Taniguchi, Role of IL-27-producing dendritic cells in Th1-immunity polarization in Lewis rats, Biochem. Biophys. Res. Commun. 338 (2005) 1773–1778.
[11] M.C. Rissoan, V. Soumelis, N. Kadowaki, G. Grouard, F. Briere, R. de Waal Malefyt, Y.J. Liu, Reciprocal control of T helper cell and dendritic cell differentiation, Science 283 (1999) 1183–1186.
[12] Z. Shen, G. Reznikoff, G. Dranoff, K.L. Rock, Cloned dendritic cells can present exogenous antigens on both MHC class I and class II molecules, J. Immunol. 158 (1997) 2723–2730.
[13] N. Okada, T. Saito, Y. Masunaga, Y. Tsukada, S. Nakagawa, H. Mizuguchi, K. Mori, Y. Okada, T. Fujita, T. Hayakawa, T. Mayumi, A. Yamamoto, Efficient antigen gene transduction using Arg-Gly-Asp fiber-mutant adenovirus vectors can potentiate antitumor vaccine efficacy and maturation of murine dendritic cells, Cancer Res. 61 (2001) 7913–7919.
[14] M. Sato, K. Iwakabe, A. Ohta, M. Sekimoto, M. Nakui, T. Koda, S. Kimura, T. Nishimura, Functional heterogeneity among bone marrow-derived dendritic cells conditioned by T(h)1- and T(h)2-biasing cytokines for the generation of allogeneic cytotoxic T lymphocytes, Int. Immunol. 12 (2000) 335–342.
[15] H. Mizuguchi, M.A. Kay, A simple method for constructing E1- and E1/E4-deleted recombinant adenoviral vectors, Hum. Gene Ther. 10 (1999) 2013–2017.
[16] Y. Kanegae, M. Makimura, I. Saito, A simple and efficient method for purification of infectious recombinant adenovirus, Jpn. J. Med. Sci. Biol. 47 (1994) 157–166.
[17] J. Nie, K. Ota, K. Morisawa, B. Auer, M. Schweiger, T. Taniguchi, Analysis of the TPA regulatory element in the genomic poly(ADP-ribose) synthetase gene in human leukemia U937 cells, Biochemistry 37 (1998) 14181–14188.

[18] M.M. Bradford, A rapid and sensitive method for the quantitation of microgram quantities of protein utilizing the principle of protein-dye binding, Anal. Biochem. 72 (1976) 248–254.
[19] M. Schnurr, T. Toy, A. Shin, M. Wagner, J. Cebon, E. Maraskovsky, Extracellular nucleotide signaling by P2 receptors inhibits IL-12 and enhances IL-23 expression in human dendritic cells: a novel role for the cAMP pathway, Blood 105 (2005) 1582–1589.
[20] M. Guha, N. Mackman, LPS induction of gene expression in human monocytes, Cell. Signal. 13 (2001) 85–94.
[21] C. Becker, S. Wirtz, X. Ma, M. Blessing, P.R. Galle, M.F. Neurath, Regulation of IL-12 p40 promoter activity in primary human monocytes: roles of NF-kappaB, CCAAT/enhancer-binding protein beta, and PU.1 and identification of a novel repressor element (GA-12) that responds to IL-4 and prostaglandin E(2), J. Immunol. 167 (2001) 2608–2618.
[22] M.B. Sewer, M.R. Waterman, Adrenocorticotropin/cyclic adenosine 3′,5′-monophosphate-mediated transcription of the human CYP17 gene in the adrenal cortex is dependent on phosphatase activity, Endocrinology 143 (2002) 1769–1777.
[23] M.B. Sewer, V.Q. Nguyen, C.J. Huang, P.W. Tucker, N. Kagawa, M.R. Waterman, Transcriptional activation of human CYP17 in H295R adrenocortical cells depends on complex formation among p54(nrb)/NonO, protein-associated splicing factor, and SF-1, a complex that also participates in repression of transcription, Endocrinology 143 (2002) 1280–1290.
[24] Y. Shav-Tal, D. Zipori, PSF and p54(nrb)/NonO–multi-functional nuclear proteins, FEBS Lett. 531 (2002) 109–114.

Neuronal Pathway from the Liver Modulates Energy Expenditure and Systemic Insulin Sensitivity

Kenji Uno,[1,2]* Hideki Katagiri,[2]*† Tetsuya Yamada,[1]* Yasushi Ishigaki,[1] Takehide Ogihara,[2] Junta Imai,[1,2] Yutaka Hasegawa,[1,2] Junhong Gao,[1,2] Keizo Kaneko,[1,2] Hiroko Iwasaki,[2] Hisamitsu Ishihara,[1] Hironobu Sasano,[3] Kouichi Inukai,[4] Hiroyuki Mizuguchi,[5] Tomoichiro Asano,[6] Masakazu Shiota,[7] Masamitsu Nakazato,[8] Yoshitomo Oka[1]

Coordinated control of energy metabolism and glucose homeostasis requires communication between organs and tissues. We identified a neuronal pathway that participates in the cross talk between the liver and adipose tissue. By studying a mouse model, we showed that adenovirus-mediated expression of peroxisome proliferator–activated receptor (PPAR)–γ2 in the liver induces acute hepatic steatosis while markedly decreasing peripheral adiposity. These changes were accompanied by increased energy expenditure and improved systemic insulin sensitivity. Hepatic vagotomy and selective afferent blockage of the hepatic vagus revealed that the effects on peripheral tissues involve the afferent vagal nerve. Furthermore, an antidiabetic thiazolidinedione, a PPARγ agonist, enhanced this pathway. This neuronal pathway from the liver may function to protect against metabolic perturbation induced by excessive energy storage.

The incidence of obesity, insulin resistance, hyperlipidemia, and hypertension, collectively referred to as the metabolic syndrome, is increasing at an alarming rate in Western cultures (*1*). Secreted humoral factors, including leptin (*2*), convey information about energy storage from adipose tissue to the central nervous system (CNS). As in adipose tissues, fat storage in the liver is dynamically changed by overall energy balance, but our understanding of how the liver transmits metabolic signals to other tissues remains incomplete. Studies of mouse models created by tissue-specific genetic engineering (*3*, *4*) or adenoviral gene transfer (*5*, *6*) have shown the importance of cross talk between tissues in the regulation of energy metabolism. Mice with tissue-specific knockout of peroxisome proliferator–activated receptor γ (PPARγ) provide an example of such intertissue communication (*7*). PPARγ activates genes involved in lipid storage and metabolism (*8*). Although PPARγ expression in the liver is low compared with that in adipose tissues (*9*), hepatic expression of PPARγ (*10*, *11*), especially that of PPARγ2 (*12*), is functionally enhanced in a number of obesity models. In addition, liver-specific disruption of PPARγ in obese (ob/ob) mice prevents hepatic steatosis but increases peripheral adiposity and decreases insulin sensitivity in muscle and fat (*13*). Thus, hepatic PPARγ2 plays important roles not only in the development of liver steatosis but also in the regulation of peripheral lipid storage and insulin sensitivity.

To investigate the mechanism by which hepatic PPARγ2 expression affects metabolism in peripheral tissues, we overexpressed PPARγ2 in the livers of C57BL/6 mice using adenoviral gene transfer. After being fed a high-fat diet for 4 weeks, the mice developed obesity-associated diabetes (*14*). The PPARγ2 adenovirus vector was then administered intravenously to mice (PPARγ2 mice). Control mice given the LacZ adenovirus (LacZ mice) showed no alterations in blood glucose levels, food intake, or plasma lipid parameters after virus administration (*14*). Systemic infusion of the PPARγ2 adenovirus into mice resulted in expression of the transgene primarily in the liver (Fig. 1A), without increased expression in peripheral tissues, including white adipose tissue (WAT) (Fig. 1B).

The livers of PPARγ2 mice were pale and enlarged as compared with those of control mice (fig. S1A). Liver weights were significantly increased (Fig. 1C) because of increased triglyceride content (Fig. 1D). Histological analysis of PPARγ2 mice revealed an abundance of large lipid droplets in the livers, without apparent inflammation or structural change (fig. S1B). Thus, hepatic PPARγ2 expression induced severe hepatic steatosis. Hepatic PPARγ2 expression enhanced the expression of lipogenesis-related genes (fig. S2), suggesting that increased uptake and synthesis of fatty acids induce severe steatosis.

In contrast, WAT in PPARγ2 mice was notably diminished in size (fig. S1A); for example, epididymal fat weight was decreased by 46.6% in PPARγ2 mice versus controls (Fig. 1E). Cell diameters in WAT and brown adipose tissue (BAT) were also markedly decreased in PPARγ2 mice (fig. S1C). The increases in body weights induced by a high-fat diet were suppressed in PPARγ2 mice (Fig. 1F). Resting oxygen consumption was increased by 29.4% in PPARγ2 mice (Fig. 1G), whereas food intake did not differ from that of LacZ mice (Fig. 1H).

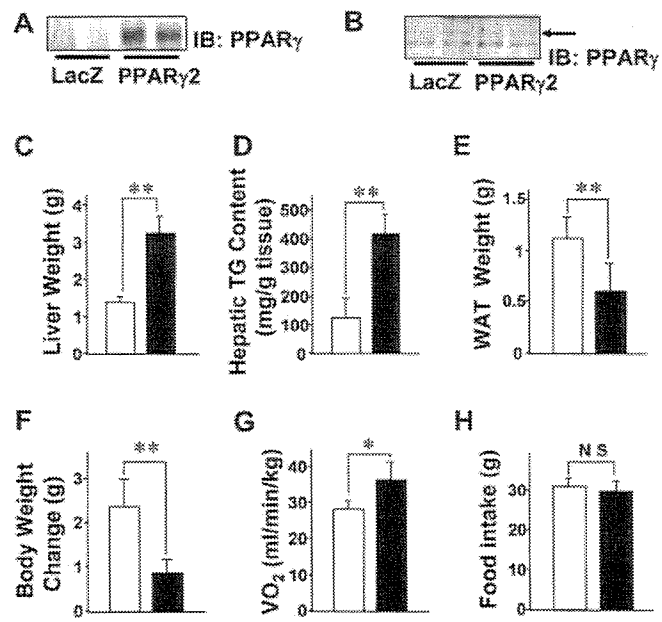

Fig. 1. Hepatic PPARγ2 expression aggravates hepatic steatosis but diminishes peripheral adiposity. (**A** and **B**) Immunoblotting (IB) with an antibody to PPARγ of liver (A) and epididymal fat (B) extracts. Liver weight (**C**), triglyceride (TG) content (**D**), and epididymal fat tissue (WAT) weights (**E**) are shown. Experiments in (A) to (E) were performed on day 7 after adenoviral administration. (**F**) Body weight changes during the 7 days after adenoviral administration. (**G**) Resting oxygen consumption (VO_2) was measured on day 3 after adenoviral injection. (**H**) Total food intake was measured for 7 days after adenoviral administration. In (C) to (H), white and black bars indicate results from LacZ mice and PPARγ2 mice, respectively. Significance as compared to LacZ mice is indicated (**$P < 0.01$ and *$P < 0.05$) by an unpaired t test. NS, not significant.

[1]Division of Molecular Metabolism and Diabetes, [2]Advanced Therapeutics for Metabolic Diseases, Center for Translational and Advanced Animal Research, [3]Department of Pathology, Tohoku University Graduate School of Medicine, Sendai 980–8575, Japan. [4]The Fourth Department of Internal Medicine, Saitama Medical School, Moroyama, Iruma-gun, Saitama 350–0495, Japan. [5]Laboratory of Gene Transfer and Regulation, National Institute of Biomedical Innovation, Osaka 567–0085, Japan. [6]Department of Physiological Chemistry and Metabolism, University of Tokyo, Tokyo 113–8655, Japan. [7]Department of Molecular Physiology and Biophysics, Vanderbilt University Medical Center, Nashville, TN 37232, USA. [8]Third Department of Internal Medicine, Miyazaki Medical College, University of Miyazaki, Kiyotake, Miyazaki 889–1692, Japan.

*These authors contributed equally to this work.
†To whom correspondence should be addressed E-mail: katagiri@mail.tains.tohoku.ac.jp

Thus, hepatic PPARγ2 expression increased systemic energy expenditure, thereby suppressing high-fat diet–induced weight gain.

Control mice were hyperglycemic, hyperinsulinemic, and hyperleptinemic in response to a 5-week-long high-fat diet. Hepatic PPARγ2 expression decreased fasting blood glucose and insulin levels (Fig. 2A), indicating markedly improved systemic insulin sensitivity. As shown in Fig. 2B, PPARγ2 mice also showed a 79% reduction in serum leptin levels. Although serum adiponectin levels were similar to those in control mice, tumor necrosis factor–α (TNF-α) levels were significantly decreased in PPARγ2 mice. These findings are consistent with a reduction in peripheral adiposity.

Glucose tolerance (Fig. 2C) and insulin tolerance (Fig. 2D) tests showed that hepatic expression of PPARγ2 markedly improved insulin sensitivity and glucose tolerance. Furthermore, improved insulin sensitivity in muscle (fig. S3A) and epididymal fat tissue (fig. S3B) was confirmed by enhanced tyrosine phosphorylation of the insulin receptor and insulin receptor substrate–1 in response to insulin administration. Thus, hepatic PPARγ2 expression clearly exerts remote beneficial effects on insulin sensitivity in muscle and WAT. Although insulin sensitivity in the liver was impaired (fig. S3C), hepatic PPARγ coactivator (PGC)–1α and hepatic phosphoenolpyruvate carboxykinase (PEPCK) expression was decreased (Fig. 2E), suggesting decreased hepatic glucose output.

To further examine insulin sensitivity and endogenous glucose production in PPARγ2 mice, we performed hyperinsulinemic euglycemic clamp experiments. Basal glucose production in PPARγ2 mice was decreased by 22% as compared with that in LacZ mice, whereas insulin's ability to suppress endogenous glucose production was severely blunted in PPARγ2 mice (Fig. 2F). In addition, glucose infusion rates in PPARγ2 mice were markedly increased (Fig. 2G). Thus, hepatic PPARγ2 expression improved insulin sensitivity in the periphery and decreased glucose output from the liver despite hepatic insulin resistance.

Serum free–fatty-acid (FFA) levels were markedly increased in PPARγ2 mice (fig. S4A), suggesting that hepatic PPARγ2 expression promotes hydrolysis of triglycerides stored in adipose tissues. Increased expression levels of the uncoupling protein (UCP)–1 (*15*), PGC1α (*16*), and hormone-sensitive lipase (*17*) in BAT (fig. S4B) and WAT (fig. S4C) indicate high tonus of the sympathetic nerves innervating these adipose tissues. In addition, the administration of bupranorol, a pan–β-adrenergic blocker (*18*), decreased serum FFA in PPARγ2 mice but had no effect in LacZ mice (fig. S4D), confirming that the β-adrenergic nerve function enhances lipolysis in adipose tissues of PPARγ2 mice.

To examine whether afferent nerves originating in the liver mediate the remote effects, we dissected the hepatic branch of the vagus nerve. Seven days after selective hepatic vagotomy (HV), we administered recombinant adenovirus encoding LacZ or PPARγ2 to mice. Hepatic PPARγ2 expression similarly altered liver weights, hepatic triglyceride content, and PEPCK expression in mice subjected to HV and sham operation (SO) (Table 1). In contrast, selective HV completely blocked the decreases in WAT weights and brown adipocyte size as well as the increases in serum FFA, resting oxygen consumption, and WAT UCP1 expression in PPARγ2 mice (Table 1), indicating that the hepatic vagus mediates the remote effects of hepatic PPARγ2 expression.

HV involves dissection of both afferent and efferent vagal branches innervating the liver. To determine whether the remote effects of hepatic PPARγ2 expression are mediated by the afferent vagus, we applied a specific afferent neurotoxin, capsaicin, to the hepatic branch of the vagus of diet-induced obese male Sprague-Dawley (SD) rats. Seven days after perivagal application of capsaicin or vehicle, we administered recombinant adenovirus encoding LacZ or PPARγ2. Expression of calcitonin gene–related peptide, a sensory neuropeptide, was markedly decreased in the capsaicin-treated vagal nerve, whereas immunoreactivity for S100 proteins was similar in vehicle- and capsaicin-treated nerves (fig. S5A). Furthermore, transmission electron microscopic analyses (fig. S5B) revealed selective degradation of unmyelinated fibers in the vagal hepatic branch. In addition, application of capsaicin to this branch did not affect the esophageal branch of the posterior vagal trunk (fig. S5). These observations indicate selective deafferentation of the hepatic branch of the vagus. Under these conditions, perivagal capsaicin treatment completely blocked the hepatic PPARγ2 expression–induced decrease in WAT weight (Table 1). When taken together, these findings strongly suggest that afferent vagal nerve ac-

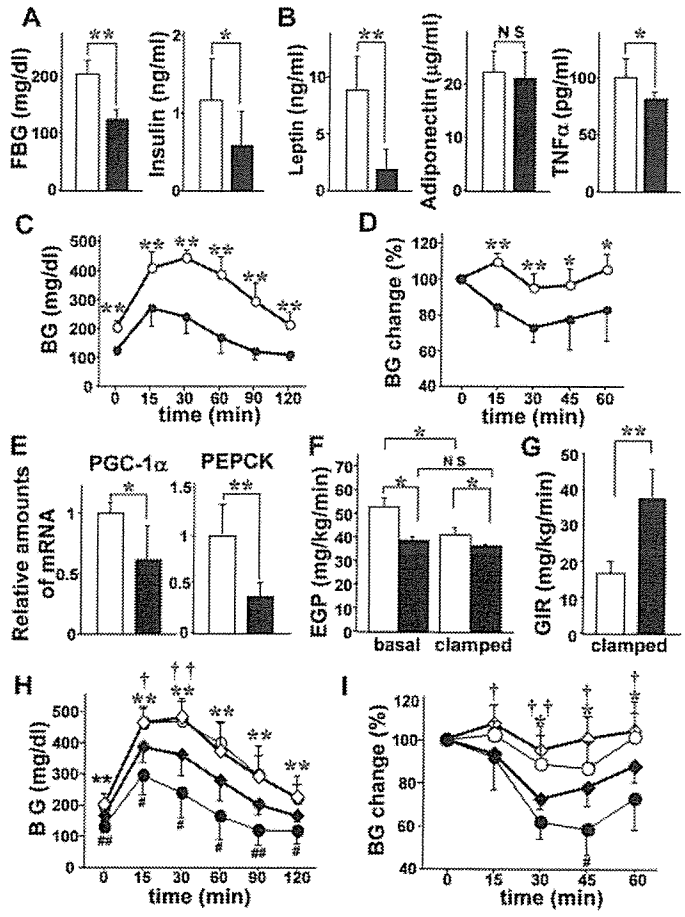

Fig. 2. Hepatic PPARγ2 expression improves peripheral insulin resistance. Fasting blood glucose (FBG) and serum insulin (**A**) and adipocytokines (**B**) were measured in LacZ mice (white bars) and PPARγ2 mice (black bars) on day 7 after adenoviral administration. These serum parameters were measured after a 10-hour fast. (**C** and **D**) LacZ mice (open circles) and PPARγ2 mice (solid circles) were subjected to glucose tolerance (C) and insulin tolerance (D) tests. BG, blood glucose. (**E**) Relative amounts of PGC-1α and PEPCK mRNA in the liver were measured by quantitative reverse transcriptase polymerase chain reaction. (**F** and **G**) Metabolic variables during hyperinsulinemic euglycemic clamp. Endogenous glucose production (EGP) in basal and clamped states (F) and rates of glucose infusion (GIR) were required to maintain euglycemia during the clamp study (G). Experiments in (A) to (G) were performed on day 7 after adenoviral administration. In (A), (B), and (E) to (G), white and black bars indicate results from LacZ mice and PPARγ2 mice, respectively. Significance as compared to LacZ mice is indicated (**$P < 0.01$ and *$P < 0.05$) by an unpaired t test. NS, not significant. (**H** and **I**) HV or SO was performed 7 days before the administration of LacZ or PPARγ2 adenovirus. Mice were subjected to glucose tolerance (H) and insulin tolerance (I) tests on day 7 after adenoviral administration. Open and solid circles indicate SO LacZ mice and SO PPARγ2 mice, respectively. Open and solid diamonds indicate HV LacZ mice and HV PPARγ2 mice, respectively. Data are presented as mean ± SD. **($P < 0.01$) and *($P < 0.05$) indicate significance in SO LacZ mice versus SO PPARγ2 mice, ††($P < 0.01$) and †($P < 0.05$) indicate significance in HV LacZ mice versus HV PPARγ2 mice, and ##($P < 0.01$) and #($P < 0.05$) indicate significance in HV PPARγ2 mice versus SO PPARγ2 mice, by unpaired t tests.

tivation originating in the liver mediates the remote effects of hepatic PPARγ2 expression on peripheral lipolysis.

We next examined the effects of HV on glucose (Fig. 2H) and insulin (Fig. 2I) tolerance test results in PPARγ2 mice. In SO mice, glucose tolerance and insulin sensitivity were improved by hepatic PPARγ2 expression, but these improvements were partially suppressed by hepatic branch vagotomy. These findings suggest that hepatic PPARγ2 expression improved glucose tolerance and systemic insulin sensitivity via both improved peripheral insulin sensitivity and decreased hepatic glucose output; the former requires afferent vagal and efferent sympathetic nerves, whereas the latter does not.

Next, to determine whether the neuronal system, consisting of afferent vagal and efferent sympathetic nerves, functions in the physiological setting of enhanced endogenous PPARγ2 expression in the liver, we examined the effects of an antidiabetic thiazolidinedione (TZD, a PPARγ agonist) using db/db mice, which are a murine model of genetic obesity and diabetes. In db/db mice, endogenous expression of PPARγ2, at both the mRNA (Fig. 3A) and the protein (fig. S6A) levels, is markedly enhanced in the liver. To eliminate the secondary effects of body weight changes, troglitazone, a TZD derivative, was given to db/db mice for 2 days, followed by an evaluation of acute effects. The TZD administration did not alter body weights (Fig. 3B) but did increase resting oxygen consumption (Fig. 3C) and UCP1 expression in BAT (Fig. 3D) and WAT (Fig. 3E), suggesting activation of sympathetic nerves to BAT and WAT. Dissection of the hepatic branch of the vagus 7 days before TZD administration reversed the increases in resting oxygen consumption (Fig. 3C) as well as UCP1 expression in BAT (Fig. 3D) and WAT (Fig. 3E). These findings indicate that the neuronal pathway originating in the liver is also involved in the acute systemic effects of TZDs, under conditions in which hepatic PPARγ expression is upregulated, such as in obese subjects.

To further examine whether endogenous PPARγ in the liver affects energy metabolism, we knocked down hepatic PPARγ in db/db mice. Administration of recombinant adenovirus expressing short hairpin RNA for PPARγ (*19*) 7 days before TZD treatment substantially decreased endogenous PPARγ expression in the liver (fig. S6B) as well as hepatic triglyceride content (fig. S6C) and sterol regulatory element binding protein–1c expression (fig. S6D), indicating functional knockdown of hepatic PPARγ (*20*). Under these conditions, TZD-enhanced energy expenditure was partially but significantly suppressed (fig. S6E). Thus, endogenous PPARγ in the liver regulates acute energy metabolism in vivo. TZD treatment reportedly alleviates insulin resistance in adipose-tissue–ablated mice (*10*) and adipose-specific-PPARγ–deficient mice (*21*), which may involve the aforementioned hepatic-PPARγ–induced neuronal activation in addition to a muscle PPARγ contribution (*22*).

We have shown that a neuronal pathway, consisting of the afferent vagus from the liver and efferent sympathetic nerves to adipose tissues, is involved in the regulation of energy expenditure, systemic insulin sensitivity, glucose metabolism, and fat distribution between the liver and the periphery. Because hepatic PPARγ expression is physiologically associated with obesity, the liver may convey information regarding excess energy balance to the CNS via the afferent vagus. This neuronal system may underlie chronic adaptive thermogenesis, resulting in protection against metabolic perturbation induced by excessive energy storage. There are two avenues of communication between the

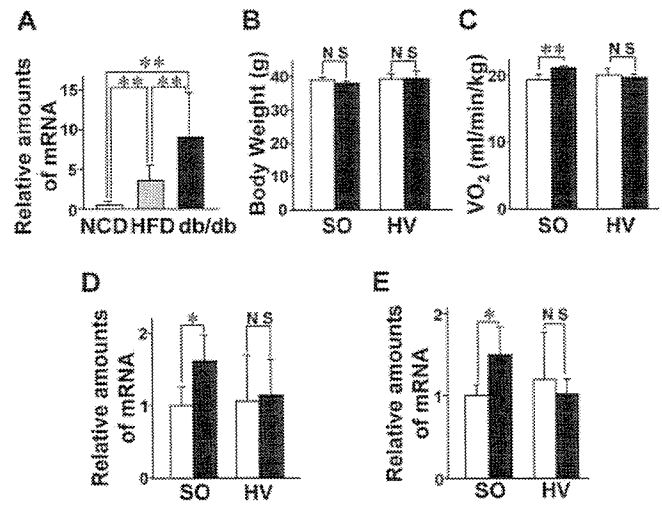

Fig. 3. HV inhibits TZD-enhanced energy expenditure in obese mice. (**A**) Relative amounts of PPARγ2 mRNA in the livers of normal chow diet–fed (NCD) C57BL/6 mice, high-fat diet–fed (HFD) C57BL/6 mice, and normal chow diet–fed db/db (db/db) mice. (**B** to **E**) db/db mice were subjected to HV or SO 7 days before the 2-day administration of TZD (black bars) or vehicle (white bars), after which body weights (B) and resting oxygen consumptions (C) were measured. Relative amounts of UCP1 mRNA in BAT (D) and epididymal fat tissue (E) from mice fed ad libitum. Data are presented as mean ± SD. Significance as compared to control mice is indicated (**$P < 0.01$ and *$P < 0.05$) by an unpaired t test. NS, not significant.

Table 1. Afferent vagal activation from the liver is involved in remote effects of hepatic PPARγ2 expression. (Upper section) Mice were subjected to HV or SO 7 days before administration of LacZ or PPARγ2 adenovirus. Resting oxygen consumption (VO_2) was measured on day 3 after adenoviral injection. Mice were killed after a 10-hour fast on day 7 after adenoviral injection. (Lower section) Male SD rats with high-fat diet–induced obesity were subjected to application of capsaicin or vehicle to the vagal hepatic branch 7 days before administration of LacZ or PPARγ2 adenovirus. Seven days after adenoviral administration, epididymal fat weights were determined. Significance as compared to LacZ mice is indicated (*P* values) by an unpaired *t* test. LW, liver weight; HTG, hepatic TG content; P, PEPCK; CD, cell diameter; NS, not significant.

	SO			HV		
	LacZ	PPARγ2	*P*	LacZ	PPARγ2	*P*
LW (g)	1.11 ± 0.13	2.30 ± 0.39	<0.001	1.12 ± 0.07	2.07 ± 0.32	<0.001
HTG (mg/g tissue)	78.71 ± 46.50	171.26 ± 43.90	0.008	62.02 ± 24.92	215.09 ± 75.78	<0.001
P mRNA (liver)	1.00 ± 0.21	0.50 ± 0.17	0.003	1.356 ± 0.460	0.54 ± 0.22	0.002
WAT weight (g)	1.13 ± 0.13	0.85 ± 0.14	<0.001	1.04 ± 0.26	1.06 ± 0.19	NS
BAT CD (μm)	11.55 ± 4.45	7.69 ± 2.09	<0.001	10.63 ± 3.38	10.55 ± 3.93	NS
FFA (μEq/l)	556.14 ± 87.33	860.47 ± 206.04	0.005	533.14 ± 59.50	558.38 ± 151.58	NS
VO_2 (ml/min/kg)	30.25 ± 2.38	34.38 ± 3.03	0.015	32.73 ± 4.54	31.98 ± 4.05	NS
UCP1 mRNA (WAT)	1.00 ± 0.24	2.36 ± 0.77	0.019	2.05 ± 0.64	1.82 ± 1.15	NS
	Vehicle			**Capsaicin**		
WAT weight (g)	8.95 ± 0.99	7.06 ± 1.32	0.024	8.70 ± 1.14	8.85 ± 1.71	NS

brain and other tissues: humoral factors and neuronal pathways. Leptin, a humoral factor from adipocytes, is a mediator of metabolic information from adipose tissue to the hypothalamus (*2*). In addition, circulating nutrients reportedly affect food intake and alter hepatic glucose production via the efferent vagal pathway (*23*, *24*). An afferent vagal signal originating in the liver is likely to be another metabolic information pathway. In this way, the brain may integrate information obtained from several tissues and organs via both humoral and neuronal pathways. When the brain receives information regarding excess energy storage, the sympathetic nervous system is activated to enhance energy expenditure and lipolysis, thereby maintaining energy homeostasis. Disturbance of the control system is implicated in the development of the metabolic syndrome (*25*). Targeting of this neuronal pathway is a potential therapeutic strategy for treating the metabolic syndrome.

References and Notes

1. J. S. Flier, *Cell* **116**, 337 (2004).
2. J. M. Friedman, J. L. Halaas, *Nature* **395**, 763 (1998).
3. Y. Minokoshi, C. R. Kahn, B. B. Kahn, *J. Biol. Chem.* **278**, 33609 (2003).
4. T. Kitamura, C. R. Kahn, D. Accili, *Annu. Rev. Physiol.* **65**, 313 (2003).
5. J. An *et al.*, *Nat. Med.* **10**, 268 (2004).
6. T. Yamada *et al.*, *Cell Metab.* **3**, 223 (2006).
7. O. Gavrilova *et al.*, *J. Biol. Chem.* **278**, 34268 (2003).
8. V. Bocher, I. Pineda-Torra, J. C. Fruchart, B. Staels, *Ann. N.Y. Acad. Sci.* **967**, 7 (2002).
9. L. Fajas *et al.*, *J. Biol. Chem.* **272**, 18779 (1997).
10. C. F. Burant *et al.*, *J. Clin. Invest.* **100**, 2900 (1997).
11. L. Chao *et al.*, *J. Clin. Invest.* **106**, 1221 (2000).
12. R. Rahimian *et al.*, *Mol. Cell. Biochem.* **224**, 29 (2001).
13. K. Matsusue *et al.*, *J. Clin. Invest.* **111**, 737 (2003).
14. Y. Ishigaki *et al.*, *Diabetes* **54**, 322 (2005).
15. I. Nagase *et al.*, *J. Clin. Invest.* **97**, 2898 (1996).
16. J. Gomez-Ambrosi, G. Fruhbeck, J. A. Martinez, *Mol. Cell. Endocrinol.* **176**, 85 (2001).
17. Y. Hatakeyama, Y. Sakata, S. Takakura, T. Manda, S. Mutoh, *Am. J. Physiol. Regul. Integr. Comp. Physiol.* **287**, R336 (2004).
18. A. Wellstein, D. Palm, G. G. Belz, *J. Cardiovasc. Pharmacol.* **8** (suppl. 11), S36 (1986).
19. T. Hosono *et al.*, *Gene* **348**, 157 (2005).
20. S. Herzig *et al.*, *Nature* **426**, 190 (2003).
21. W. He *et al.*, *Proc. Natl. Acad. Sci. U.S.A.* **100**, 15712 (2003).
22. A. L. Hevener *et al.*, *Nat. Med.* **9**, 1491 (2003).
23. A. Pocai, S. Obici, G. J. Schwartz, L. Rossetti, *Cell Metab.* **1**, 53 (2005).
24. T. K. Lam *et al.*, *Nat. Med.* **11**, 320 (2005).
25. M. W. Schwartz, D. Porte Jr., *Science* **307**, 375 (2005).

26. We thank M. Kaji, T. Takai, Y. Sato, H. Yawo, T. Hashikawa, M. Kanzaki, Y. Minokoshi, and M. Tominaga for advice and discussions. Supported by grants-in-aid from the Ministry of Education, Science, Sports, and Culture of Japan (H.K.), a grant-in-aid from the Ministry of Health, Labor, and Welfare of Japan (Y.O.), and the 21st Century Center of Excellence Programs (H.K. and Y.O.).

Supporting Online Material

www.sciencemag.org/cgi/content/full/312/5780/1656/DC1
Materials and Methods
SOM Text
Figs. S1 to S6
Table S1
References

9 February 2006; accepted 8 May 2006
10.1126/science.1126010

Synaptic Amplifier of Inflammatory Pain in the Spinal Dorsal Horn

Hiroshi Ikeda,* Johanna Stark, Harald Fischer, Matthias Wagner, Ruth Drdla, Tino Jäger, Jürgen Sandkühler†

Inflammation and trauma lead to enhanced pain sensitivity (hyperalgesia), which is in part due to altered sensory processing in the spinal cord. The synaptic hypothesis of hyperalgesia, which postulates that hyperalgesia is induced by the activity-dependent long-term potentiation (LTP) in the spinal cord, has been challenged, because in previous studies of pain pathways, LTP was experimentally induced by nerve stimulation at high frequencies (~100 hertz). This does not, however, resemble the real low-frequency afferent barrage that occurs during inflammation. We identified a synaptic amplifier at the origin of an ascending pain pathway that is switched-on by low-level activity in nociceptive nerve fibers. This model integrates known signal transduction pathways of hyperalgesia without contradiction.

Inflammation of peripheral tissues causes spontaneous pain and hyperalgesia. Amplification of pain-related information in the spinal dorsal horn lamina I contributes to inflammatory pain (*1*–*6*). Inflammation causes release of neuromodulators, including substance P and glutamate in spinal dorsal horn (*7*, *8*), potentially leading to Ca^{2+}-dependent LTP. In all previous studies, spinal LTP was induced by brief (1 s), high-frequency (100 Hz) burstlike stimulation (HFS) of afferent nerve fibers. High-frequency bursts do not, however, resemble the continuous low-frequency afferent barrage that occurs during inflammation. Low-frequency presynaptic activity normally fails to induce LTP but rather induces synaptic long-term depression (LTD) (*9*). The LTP model of inflammatory hyperalgesia thus may be questioned. Here, we evaluated the effect of low-frequency afferent barrage on synaptic transmission in ascending pain pathways and asked if synaptic plasticity is differentially induced in distinct ascending pain tracts. We labeled lamina I projection neurons by retrograde fluorescent marker DiI (1,1′-dioctadecyl-3,3,3′,3′-tetramethylindocarbocyanine perchlorate), injected into either of two major projection areas of spinal lamina I neurons: the parabrachial (PB) area or the periaqueductal gray (PAG) (*10*, *11*) (Fig. 1, A and B). To circumvent confounding developmental factors, we used only juvenile or adult rats in this study. Transverse spinal cord slices with long dorsal roots attached were prepared 3 to 4 days after DiI injections to allow whole-cell recordings from identified projection neurons in 21- to 28-day-old rats (*10*). In the presence of tetrodotoxin, bath application of substance P (2 μM) induced transient inward currents in 21 out of 27 spino-PB and in 9 out of 12 spino-PAG neurons (Fig. 1C), confirming the expression of functional neurokinin 1 receptors (NK1Rs). Spinal release of substance P following electrical stimulation of primary afferents at C-fiber strength was assessed by the internalization of NK1R in lamina I neurons. HFS parameters (100-Hz bursts) similar to all previously used conditioning stimulation protocols to induce classical LTP in pain pathways, or low-frequency stimulation (LFS, 2 Hz), was used. Both types of stimulation elicited substantial NK1R internalization in 89 ± 1% and in 78 ± 4% of 150 neurons evaluated in three rats per group (Fig. 1D). We then used these stimulation protocols for conditioning.

Conditioning HFS induces LTP at synapses between C-fibers and lamina I neurons that project to the PB (*12*). We confirmed these results by showing LTP of monosynaptically evoked excitatory postsynaptic currents (EPSCs) to 172 ± 15% of the control value at 30 min after conditioning (n = 8) (Fig. 2A). However, conditioning electrical stimulation within the typical frequency band of C-fibers during inflammation (2 Hz) (*13*) did not change synaptic strength in any of the spino-PB neurons tested (108 ± 19% of control, n = 7) (Fig. 2C). LFS, however, did modify synaptic strength in spinal lamina I neurons with a projection to the PAG. In all spino-PAG neurons tested, LFS induced a robust LTP of monosynaptic C-fiber–evoked EPSCs [to 262 ± 30% of the control value at 30 min after stimulation (n = 18) and to 346 ± 33% at 60 min (n = 8)] (Fig. 2D). In all seven lamina I neurons with a projection to the PAG, conditioning stimulation at high frequency was ineffective (98 ± 10%, n = 7) (Fig. 2B). Monosynaptic, A-fiber–evoked

Department of Neurophysiology, Center for Brain Research, Medical University of Vienna, Vienna, Austria.

*Present address: Department of Human and Artificial Intelligence Systems, University of Fukui, 3-9-1 Bunkyo, Fukui 910-8507, Japan.

†To whom correspondence should be addressed. E-mail: juergen.sandkuehler@meduniwien.ac.at

nature medicine

In vivo imaging of lymph node metastasis with telomerase-specific replication-selective adenovirus

Hiroyuki Kishimoto[1,2], Toru Kojima[1,2], Yuichi Watanabe[1,3], Shunsuke Kagawa[1,2], Toshiya Fujiwara[1,2], Futoshi Uno[1,2], Fuminori Teraishi[1,2], Satoru Kyo[4], Hiroyuki Mizuguchi[5], Yuuri Hashimoto[3], Yasuo Urata[3], Noriaki Tanaka[1] & Toshiyoshi Fujiwara[1,2]

Currently available methods for detection of tumors *in vivo* such as computed tomography and magnetic resonance imaging are not specific for tumors. Here we describe a new approach for visualizing tumors whose fluorescence can be detected using telomerase-specific replication-competent adenovirus expressing green fluorescent protein (GFP) (OBP-401). OBP-401 contains the replication cassette, in which the human telomerase reverse transcriptase (hTERT) promoter drives expression of *E1* genes, and the *GFP* gene for monitoring viral replication. When OBP-401 was intratumorally injected into HT29 tumors orthotopically implanted into the rectum in BALB/c *nu/nu* mice, para-aortic lymph node metastasis could be visualized at laparotomy under a three-chip color cooled charged-coupled device camera. Our results indicate that OBP-401 causes viral spread into the regional lymphatic area and selectively replicates in neoplastic lesions, resulting in GFP expression in metastatic lymph nodes. This technology is adaptable to detect lymph node metastasis *in vivo* as a preclinical model of surgical navigation.

Medical imaging techniques have become an essential aspect of cancer diagnosis, detection, and treatment monitoring. Advances and improvements in the major imaging modalities such as computed tomography, magnetic resonance imaging and ultrasound techniques have increased the sensitivity of visualizing tumors and their metastases in the body[1,2]. A limiting factor of these techniques is, however, the inability to specifically identify malignant tissues. Positron emission tomography with the glucose analog ^{18}F-2-deoxy-D-glucose is the first molecular imaging technique that has been widely applied for cancer imaging in clinical settings[3]. Although ^{18}F-2-deoxy-D-glucose–positron emission tomography has high detection sensitivity, it has some limitations such as the difficulty in distinguishing between proliferating tumor cells and inflammation and the inability in using it for real-time detection of tumor tissues. A relatively inexpensive, robust and straightforward way of defining the location and area of tumors *in vivo* would greatly aid the treatment of human cancer, especially for surgical procedures. In particular, if tumors too small for direct visual detection and therefore not detectable by direct inspection could be imaged *in situ*, surgeons could excise such tumors precisely with appropriate surgical margins.

Sentinel lymph node (SLN) mapping is a minimally invasive procedure and widely used in the management of patients with cutaneous melanoma or breast cancer without clinical evidence of nodal metastases[4,5]. The technique assumes that early lymphatic metastases, if present, are always found first within the SLN, the first tumor-draining lymph node. A SLN free of tumor cells would therefore predict the absence of metastatic disease in the rest of the tumor-draining lymph node basin, which indicates that intensive lymphadenectomy is unlikely to benefit those patients. Several studies have validated this assumption; the sensitivity of intraoperative frozen-section analysis for detection of nodal metastases, however, is relatively low, and high false-negative rates have been reported[6–9]. In addition, thicker primary and larger SLN tumor size has been shown to be predictive of non-SLN metastasis, presumably because of the altered lymphatic drainage routes. These findings raise doubt about the applicability of this technique in widespread surgical practice; therefore, several different approaches have been taken to directly label tumor cells to visualize and track them *in vivo*.

The GFP, which was originally identified from the jellyfish *Aequorea victoria*, is an attractive molecular marker for imaging in live tissues because of the relatively noninvasive nature of fluorescence[10–15]. We previously demonstrated a real-time fluorescence optical imaging of pleural dissemination of human non-small-cell lung cancer cells in an orthotopic mouse model using tumor-specific replication-competent adenovirus (OBP-301, Telomelysin)[16,17] in combination with replication-deficient adenovirus expressing *GFP* (Ad-*GFP*)[18]. In the present study we additionally modified OBP-301 to contain the *GFP* gene driven by the cytomegalovirus (CMV) promoter for monitoring viral replication. The resultant adenovirus, termed OBP-401, efficiently labeled tumor cells with green fluorescence *in vitro* and *in vivo*. The results showed that injection of OBP-401 into primary tumors allows its lymphatic spread, which in turn induces viral replication in

[1]Division of Surgical Oncology, Department of Surgery, Okayama University Graduate School of Medicine, Dentistry and Pharmaceutical Sciences, 2-5-1 Shikata-cho, Okayama 700-8558, Japan. [2]Center for Gene and Cell Therapy, Okayama University Hospital, 2-5-1 Shikata-cho, Okayama 700-8558, Japan. [3]Oncolys BioPharma, Inc., 3-16-33 Roppongi, Minato-ku, Tokyo 106-0032, Japan. [4]Department of Obstetrics and Gynecology, Kanazawa University School of Medicine, 13-1 Takara-machi, Kanazawa 920-8641, Japan. [5]Laboratory of Gene Transfer and Regulation, National Institute of Biomedical Innovation, 7-6-8 Saito-Asagi, Ibaraki, Osaka 567-0085, Japan. Correspondence should be addressed to T.F. (toshi_f@md.okayama-u.ac.jp).

Received 9 February; accepted 3 April; published online 1 October 2006; doi:10.1038/nm1404

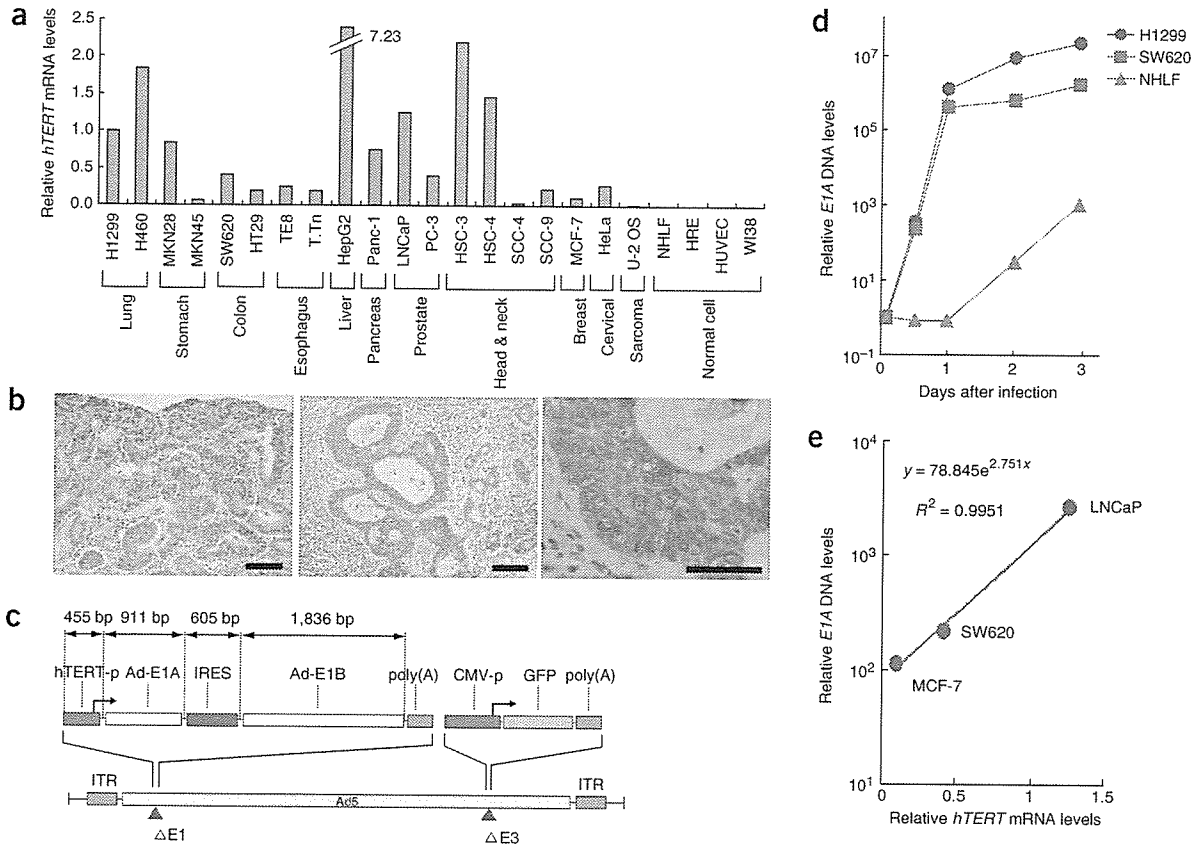

Figure 1 hTERT expression and selective replication of OBP-401 in human cancer cells. (**a**) Relative *hTERT* mRNA expression in human tumor and normal cell lines determined by real-time RT-PCR analysis. The *hTERT* mRNA expression of H1299 human lung cancer cells was considered as 1.0, and the relative expression of each cell line was calculated against that of H1299 cells. (**b**) Immunohistochemical analysis of the hTERT protein expression in surgical specimens of human gastric cancer and their microscopic metastases in lymph nodes. Representative microscopic images of primary tumor (left panel) and metastatic foci in lymph node (middle and right) are shown. Positive staining is reddish brown. Counterstain is blue-purple. Original magnification: ×200 (left and middle) and ×400 (right). Scale bar, 100 μm. (**c**) DNA structures of OBP-401. (**d**) Assessment of viral DNA replication in H1299, SW620 and NHLF cells. Cells were infected with OBP-401 at an MOI of 10 for 2 h. Subsequent to the removal of virus inocula, cells were additionally incubated for the indicated time periods and then subjected to real-time quantitative PCR assay. The amounts of viral E1A copy number are defined as the fold increases for each sample relative to that at 2 h (2 h equals 1). (**e**) Relationship between viral replication and hTERT expression determined by real-time RT-PCR analysis. Plots represent the relative *E1A* DNA levels at 24 h after OBP-401 infection and the relative *hTERT* mRNA levels in SW620, LNCaP and MCF-7 cell lines. The slope represents the positive correlation between these two factors ($R^2 = 0.9951$).

metastatic lymph nodes, thereby leading to the direct imaging of micrometastases. This technology is adaptable to detect lymph node metastasis *in vivo* as a preclinical model of surgical navigation.

RESULTS

hTERT levels in human cell lines and lymph node metastases

To confirm the specificity of telomerase activity in human cancer cells, we measured expression of *hTERT* mRNA in a panel of human tumor and normal cell lines using a real-time RT-PCR method. Although the expression varied widely, all tumor cell lines derived from different organs expressed detectable levels of *hTERT* mRNA, whereas human fibroblast cells lines such as the normal human lung fibroblast (NHLF) and normal human lung diploid fibroblast (WI38), human vascular endothelial cells, and normal human renal epithelial cells were negative for *hTERT* expression (**Fig. 1a**). We also examined samples of 30 primary tumors and 39 lymph node metastases obtained from gastric cancer patients for hTERT protein expression by immunohistochemistry (**Supplementary Table 1** online). As shown in **Fig. 1b**, hTERT staining was clearly observed in metastatic foci of gastric cancers, although most of the lymphocytes present in lymph nodes were negative for hTERT except in some germinal centers. These results suggest that the hTERT promoter element can be used to target human cancer.

Selective visualization of human cancer cells *in vitro*

We constructed the tumor-specific replication-competent adenovirus OBP-401, which expresses *GFP* by inserting the *GFP* gene under the control of the CMV promoter at the deleted E3 region of the telomerase-specific replication-selective type 5 adenovirus OBP-301 (refs. 16,17) (**Fig. 1c**). To evaluate the replication ability of OBP-401 in different cell lines, we measured the relative amounts of *E1A* DNA by quantitative real-time PCR analysis. Human cancer cells (H1299 and SW620) and normal cells (NHLFs) were infected with OBP-401 at a multiplicity of infection (MOI) of 10 for 2 h, followed by incubation in the medium. Cells were harvested at various times during the 3 d after infection, and the virus yield was determined by quantitative real-time PCR assay targeting for the viral *E1A* sequence. The ratios were normalized by dividing the value of cells obtained 2 h after viral infection. In SW620 and H1299 cells, OBP-401 replicated 6–7 logs by 3 d after infection;

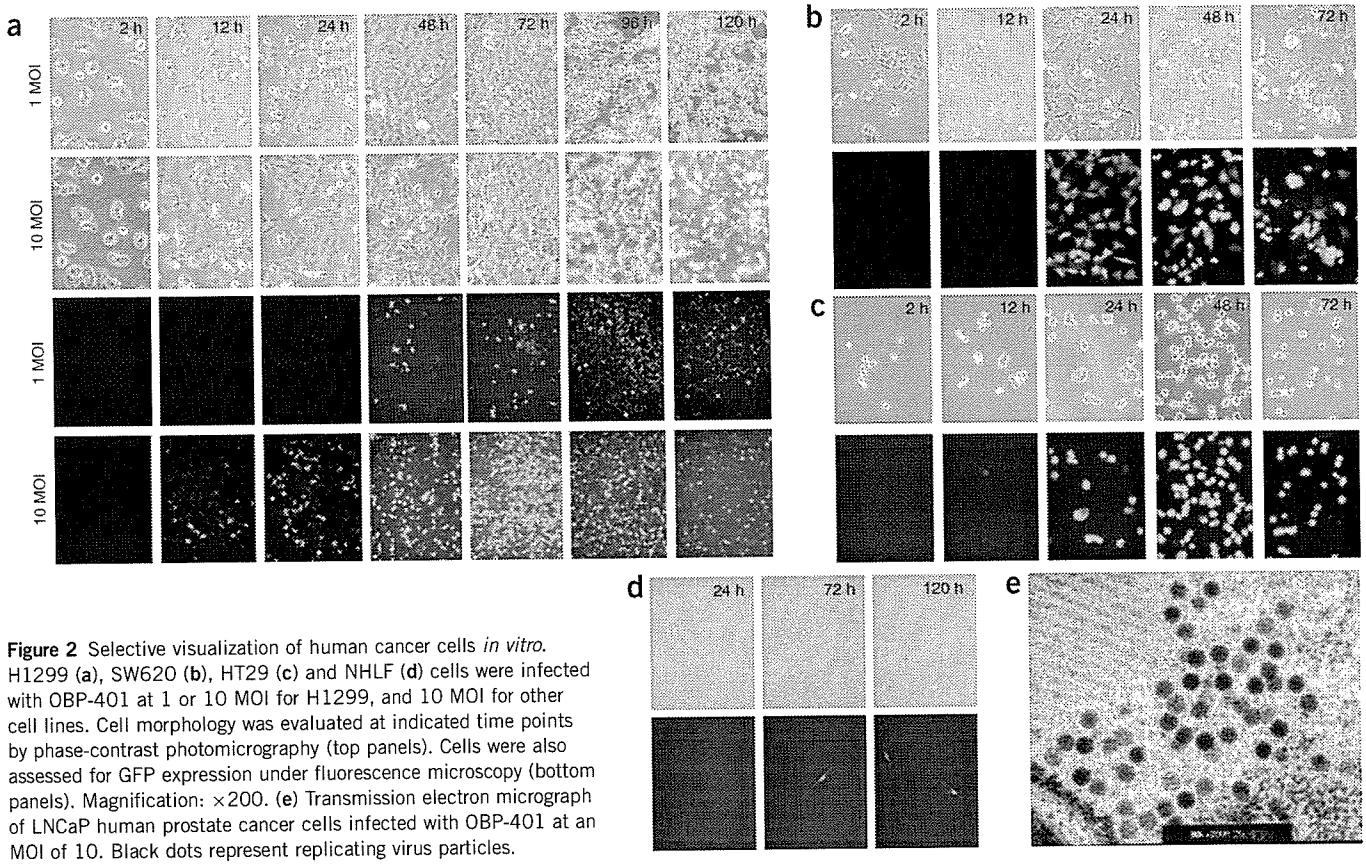

Figure 2 Selective visualization of human cancer cells *in vitro*. H1299 (**a**), SW620 (**b**), HT29 (**c**) and NHLF (**d**) cells were infected with OBP-401 at 1 or 10 MOI for H1299, and 10 MOI for other cell lines. Cell morphology was evaluated at indicated time points by phase-contrast photomicrography (top panels). Cells were also assessed for GFP expression under fluorescence microscopy (bottom panels). Magnification: ×200. (**e**) Transmission electron micrograph of LNCaP human prostate cancer cells infected with OBP-401 at an MOI of 10. Black dots represent replicating virus particles.

OBP-401 replication, however, was attenuated up to 3 logs in normal NHLFs (**Fig. 1d**). These findings indicate that OBP-401 viral recovery was reduced by 3–4 logs in normal cells as compared with cancer cells. We also found an apparent correlation between viral yields at 24 h after OBP-401 infection and *hTERT* mRNA expression in human cancer cell lines (**Fig. 1e**).

To determine whether OBP-401 replication is associated with selective GFP expression, cells were analyzed and photographed by fluorescent microscope after OBP-401 infection. As shown in **Fig. 2a**, H1299 human non-small-cell lung cancer cells expressed bright GFP fluorescence as early as 12 h after OBP-401 infection at an MOI of 10. The fluorescence intensity gradually increased in a dose-dependent fashion until ~72 h after infection, followed by rapid cell death due to the cytopathic effect of OBP-401, as shown by floating, highly light-refractile cells under phase-contrast photomicrographs. In SW620 and HT29 human colorectal cancer cells we detected GFP expression 24 h after infection with 10 MOI of OBP-401, and cells showed the cytopathic effect at 72 h after infection (**Fig. 2b,c**). In contrast, normal NHLF cells were negative for GFP expression after OBP-401 infection (**Fig. 2d**). These results indicate that OBP-401 can replicate exclusively in human cancer cells, leading to tumor cell–specific GFP fluorescence expression *in vitro*. We detected replicating virus particles in human cancer cells by transmission electron microscopy (**Fig. 2e**). The cytopathic effect of OBP-401 was also assessed by the cell viability assay using the tetrazolium salt XTT. In both SW620 and HT29 cells, OBP-401 infection induced rapid cell death in a dose-dependent manner (**Supplementary Fig. 1a** online). In *nu/nu* mice carrying subcutaneous SW620 human colorectal tumor xenografts, intratumoral injection of OBP-401 resulted in a significant inhibition of tumor growth as compared with mock-treated tumors (**Supplementary Fig. 1b** online).

Selective visualization of subcutaneous tumors *in vivo*

It is reported that the hTERT promoter could be used to induce transgene expression in syngenic tumors in mice[19]. We first confirmed that OBP-401 could replicate and express GFP fluorescence in Colon-26 cells *in vitro* as well as *in vivo* (**Supplementary Fig. 2a,b** online). In contrast, OBP-401 replication was attenuated in mouse splenocytes (**Supplementary Fig. 2a** online). These results suggest that the hTERT promoter can efficiently use the mouse transcriptional machinery and, therefore, the selectivity of OBP-401 can be examined in human tumor xenografts in mice.

To assess the specificity of the GFP-based fluorescent optical detection of tumors *in vivo*, we examined the kinetics of GFP transgene expression in subcutaneous SW620 and HT29 tumors after intratumoral injection of 1×10^7 PFU per 100 μl of OBP-401 with the charged-coupled device (CCD) noninvasive imaging system. Whole-body images of mice showed that intratumoral GFP fluorescence signals were detectable within 24 h after local delivery of viruses (**Fig. 3a**). The fluorescence intensity reached maximum levels within 4 d after injection and was maintained for at least 7 d. When SW620 tumors were removed 14 d after intratumoral injection of OBP-401, the high GFP transgene expression was visible on the surface of tumors as well as across serially sliced sections (**Fig. 3b**). No GFP fluorescence was detected when non-tumor-bearing mice were subcutaneously injected with 1×10^7 PFU per 100 μl of OBP-401 (**Fig. 3c**), suggesting confinement of GFP expression to the tumor.

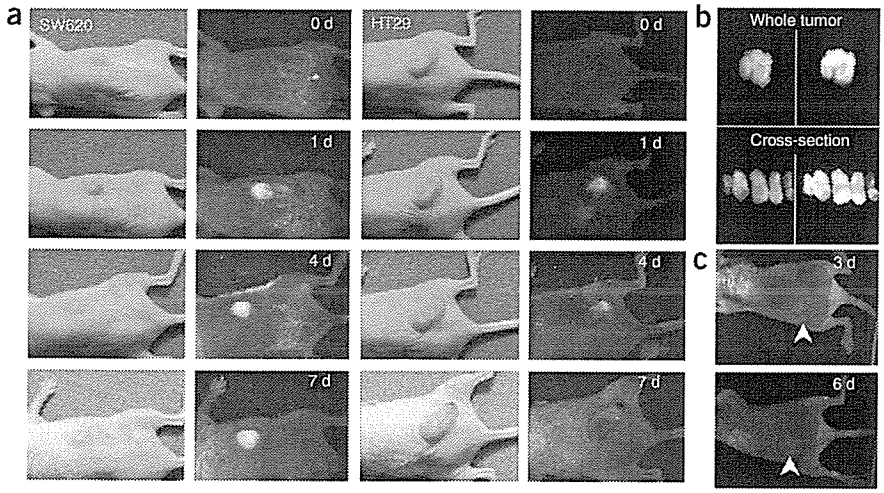

Figure 3 Selective visualization of subcutaneous tumors *in vivo*. (**a**) Time course of external images of subcutaneous SW620 and HT29 tumors after intratumoral injection of OBP-401. When tumors grew to ~6–7 mm in diameter after subcutaneous inoculation of SW620 and HT29 tumor cells (5×10^6 cells per mouse), OBP-401 viruses at the concentration of 1×10^7 PFU were directly injected into established tumors. The GFP fluorescence intensity was monitored for 7 d under the CCD noninvasive imaging system. Left panels, macroscopic appearance of subcutaneous tumors; right panels, fluorescence detection. (**b**) SW620 tumors were excised 14 d after OBP-401 injection and then assessed for GFP fluorescence as a whole tumor or in cross-sections. Left panels, macroscopic appearance of subcutaneous tumors; right panels, fluorescence detection. (**c**) Photographs of non-tumor-bearing *nu/nu* mice injected with OBP-401. Mice were subcutaneously injected with 1×10^7 PFU of OBP-401 and documented as photographs for GFP expression 3 d and 6 d after injection. Arrowheads, injected area.

Orthotopic mouse model of human rectal cancer with metastasis

The development of the orthotopic implantation technique for human rectal cancer has been described[20]. Our preliminary experiments revealed that, when 5×10^6 HT29 human colorectal cancer cells suspended in Matrigel are inoculated into the rectum submucosa of athymic *nu/nu* mice, rectal tumors appeared within 7 d after tumor injection (**Fig. 4a,b**). Histopathological examination of the excised primary tumor showed a submucosal tumor formation composed of implanted HT29 cells with a solid architecture and invasion into the muscularis propria and submucosa (**Fig. 4c**). Examination under high magnification showed tumor cell–filled lymphatic vessels in the muscularis propria layer (**Fig. 4c**). As expected, we detected the green fluorescence expression from 24 h after intratumoral administration of OBP-401 in the primary rectal tumors, with maximum signal occurring 2–4 d after injection, whereas tumors not injected with OBP-401 were completely GFP negative (**Fig. 4d**).

Selective visualization of lymph node metastasis

In our preliminary experiments, we confirmed that most mice with rectal tumors subsequently developed lymph node metastasis around the abdominal aorta from the lower margin of the renal vein to the aortic bifurcation, which were microscopically detectable ~4 weeks after tumor inoculation. Five days after injection of 1×10^8 PFU of OBP-401 into the implanted rectal tumors, we explored the abdominal cavity at laparotomy. Analyses of two representative mice are shown in **Figure 4**. Three lymph nodes (LN1, LN2 and LN3) were macroscopically identified adjacent to the aorta (**Fig. 4e,f**); the optical CCD imaging of the abdominal cavity, however, demonstrated that only one lymph node (LN3) could be detected as light-emitting spots with GFP fluorescence (**Fig. 4f**). In the other mouse, three of four lymph nodes could be imaged as GFP signals (**Fig. 4h**). We detected no GFP fluorescence in abdominal lymph nodes after injection of 1×10^7 PFU of OBP-401 into the rectal tumors (data not shown). Histopathological analysis confirmed the presence of metastatic adenocarcinoma cells in the lymph nodes with fluorescence emission, whereas GFP-negative lymph nodes contained no tumor cells (**Fig. 4g,i**). In addition, immunohistochemical analysis for GFP protein demonstrated that the reddish brown GFP-immunoreactive cells corresponded to the microscopic metastatic nodules in the lymph nodes but were not detected in the nonmetastatic lymphocyte area (**Supplementary Fig. 3** online).

We verified the GFP-based fluorescence detection with OBP-401 and histological correlation of lymph node metastasis in a series of *in vivo* experiments. Representative examples of the data are summarized in **Table 1**. Among the 7 tumor-bearing mice, 6 mice (85.7%) developed histologically confirmed lymph node metastasis. Of 28 lymph nodes excised from 7 mice, histopathological analysis demonstrated that 13 nodes (46.4%) contained micrometastatic nodules. The optical CCD imaging detected 12 lymph nodes labeled in spots with GFP fluorescence in 13 metastatic nodes (sensitivity of 92.3%). Among 15 metastasis-free lymph nodes, 2 nodes were GFP positive (specificity of 86.7%). Our results indicate that intratumoral injection of OBP-401 causes viral spread into the regional lymphatic area and selective replication in cancer cells in metastatic lymph nodes, which in turn could be imaged with GFP fluorescence. Moreover, the finding that OBP-401 did not express GFP fluorescence in a mouse para-aortic lymphadenitis model induced by inoculating complete Freund adjuvant into the rectum submucosa of

Table 1 GFP fluorescence and histopathology status in para-aortic lymph nodes of HT29 tumor-bearing mice

		GFP fluorescence[b]		
Mouse no.	Metastasis[a]	Positive	Negative	Total (%)[c]
1	Positive	1	0	1 (33.3)
	Negative	0	2	2 (66.6)
2	Positive	3	0	3 (75.0)
	Negative	0	1	1 (25.0)
3	Positive	1	0	1 (33.3)
	Negative	0	2	2 (66.6)
4	Positive	0	0	0 (0)
	Negative	0	4	4 (100)
5	Positive	1	1	2 (66.6)
	Negative	0	1	1 (33.3)
6	Positive	3	0	3 (60.0)
	Negative	1	1	2 (40.0)
7	Positive	3	0	3 (50.0)
	Negative	1	2	3 (50.0)

[a]Metastatic foci were detected histologically by hematoxylin and eosin staining. [b]Nodes with light-emitting spots and GFP fluorescence were evaluated as positive. [c]The percentage of nodes with or without histologically confirmed metastasis in each mouse.

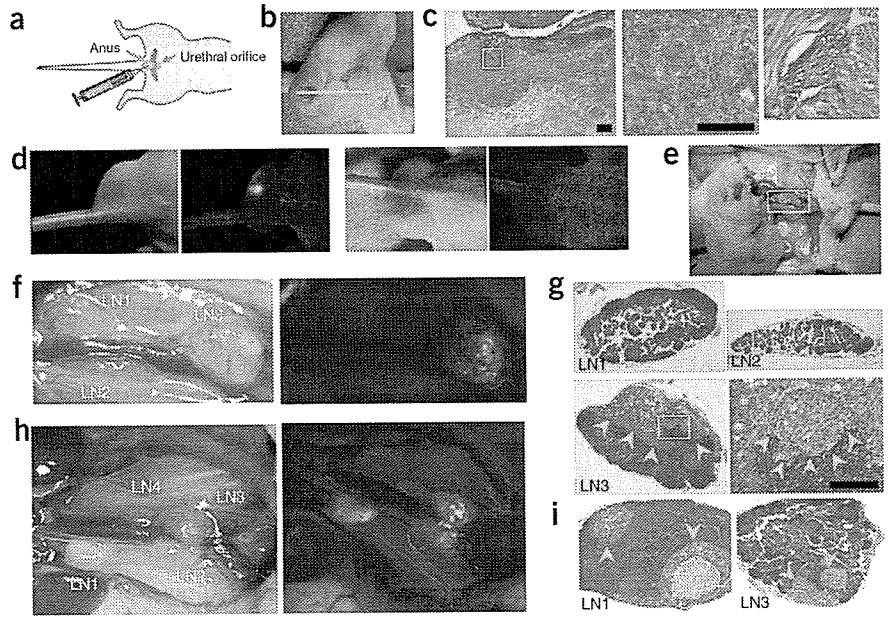

Figure 4 Orthotopic xenografts of human colorectal cancer cells and selective visualization of lymph node metastasis in two representative mice (no. 1 and no. 2). (**a**) Method used to produce HT29 human rectal tumors in BALB/c *nu/nu* mice. The rectums of mice were inoculated with 5×10^6 HT29 cells. (**b**) Macroscopic appearance of HT29 rectal tumor 4 weeks after tumor inoculation. Mice were killed and subjected to autopsy. Green line, the direction of tumor cross-sections. (**c**) Histologic sections stained with H&E showing local growth of HT29 tumor in the submucosal layer of the rectum. Scale bar, 100 μm. Left, magnification: ×40; middle (detail of the boxed region of left panel), magnification: ×400; right, lymphatic vessel invasion of HT29 tumor cells (arrowhead), magnification: ×400. (**d**) External images of orthotopic HT29 tumor-bearing *nu/nu* mice injected with OBP-401. OBP-401 at the concentration of 1×10^8 PFU were directly injected into implanted HT29 tumor (left). The GFP fluorescence could be detected as early as 24 h after OBP-401 injection under CCD imaging. Macroscopic and fluorescent images of HT29 tumor without OBP-401 injection (right). (**e**) Gross appearance of the abdominal cavity (mouse no. 1). At 5 d after intratumoral injection of OBP-401 at the concentration of 1×10^8 PFU, HT29 tumor-bearing *nu/nu* mice were assessed for lymph node metastasis at laparotomy. The white box outlines a region of **f**. (**f**) Three para-aortic lymph nodes were identified in mouse no. 1 (LN1, LN2 and LN3) (left). Internal imaging with the optical CCD camera visualized one of three nodes with GFP fluorescence (LN3) (right). (**g**) H&E staining of lymph node sections. Lymph nodes without metastatic tumors (LN1 and LN2). Lymph node containing metastatic tumors (arrowheads) (LN3) (Left, magnification: ×200; right, magnification: ×400). Scale bar, 100 μm. (**h**) Four para-aortic lymph nodes were identified in mouse no. 2 (LN1, LN2, LN3 and LN4) (left). Three of four nodes were positive for light-emitting spots with GFP fluorescence (LN1, LN2 and LN3) (right). (**i**) Histopathological detection of metastatic foci in nodes (LN1 and LN3) (arrowheads).

immunocompetent BALB/c mice suggests that this strategy could distinguish cancer metastasis from inflammatory lymphadenopathy (**Supplementary Fig. 4** online).

DISCUSSION

Lymph node status provides important information for both the diagnosis and treatment of human cancer[21,22]. Lymphatic invasion is one of the major routes for cancer cell dissemination, and adequate resection of locoregional lymph nodes is required for curative treatment in patients with advanced malignancies. The risk of having lymph node metastasis can be partially predicted by clinical data such as tumor stage, serum tumor marker concentration and medical images; there are, however, no noninvasive approaches to accurately predict the presence of lymph node metastasis, in particular, microscopic metastasis.

The specific aim of the present study was to determine the suitability of telomerase-specific amplification of the *GFP* gene for real-time imaging tumor tissues and, if so, detect nodal metastasis *in vivo* before the traditional, cumbersome procedures of histopathological examination. GFP-based fluorescence imaging can allow real-time detection of target cells without time-consuming steps such as fixation and tissue processing[13–15]. Indeed, Yang *et al.* have shown that GFP-expressing tumors growing and metastasizing in intact animals could be viewed externally with a whole-body optical imaging system[13]. Moreover, the *GFP* gene could be delivered to metastatic tumor cells *in vivo* by viral vectors[14].

To distinguish normal from neoplastic tumor tissues, selective labeling of tumor cells is required. OBP-401 produced a viral yield of 6–7 logs in human cancer cells within 3 d of infection, which was 3–4 logs higher than that in normal cells, suggesting the reliable tumor selectivity of OBP-401. Although the reason why OBP-401 replicated slightly in NHLFs despite the lack of *hTERT* mRNA expression is unclear, the fact that NHLFs could be maintained in the culture up to passages 10–20 indicates that NHLFs might have a weak telomerase activity that is undetectable by standard PCR assay. However, the attenuated replication property of OBP-401 in normal cells seems not to interfere with the visualization of tumor cells *in vivo*. In fact, we detected no GFP expression in adjacent normal tissues in subcutaneous human cancer xenografts after intratumoral injection of OBP-401, although the cross-sections of the tumor were entirely imaged with GFP fluorescence. Thus, OBP-401 provides possible probing of tumor cells *in vivo*.

Experiments using a three-CCD optical imaging system demonstrated that metastatic lymph nodes could be detected at laparotomy in mice 5 d after OBP-401 injection into implanted primary human rectal tumors. Notably, metastatic lymph nodes were imaged in spots with GFP fluorescence, which coincided with histologically confirmed micrometastasis. This experiment mimics the clinical scenario in which patients with gastrointestinal malignancies with lymph node metastasis undergo surgery, and the data suggest that the surgeon can identify metastatic lymph nodes by illuminating the abdominal cavity with a xenon lamp. The sensitivity and specificity of this imaging strategy are 92.3% and 86.7%, respectively; these results are sufficiently reliable to support the concept of this approach. In our phase I trial of a replication-deficient adenovirus vector expressing the wild-type *p53* gene (AdCMV-*p53*, ADVEXIN), DNA-PCR analysis targeting the viral genome indicated that the virus was present in tumor tissue as well as proximal lymph nodes, suggesting regional spread of the vector via the lymphatic vessels[23]. Therefore, OBP-401 is likely to be accessible to the regional lymph nodes via intratumoral administration in humans.

Currently, analysis of lymph nodes with H&E staining and microscopic examination usually involves review of only one or two tissue sections, and small foci of tumor cells can be missed. For intraoperative frozen-section analysis of SLNs, this underestimation is even more pronounced as a result of poor tissue architecture. In the treatment of breast cancer and melanoma, in which SLN biopsy is commonly used, the sensitivity of intraoperative frozen-section analysis ranges from 38% to 74% (refs. 6–9). In our experiments, additional serial sectioning was needed in 4 of 12 (33.3%) lymph nodes with GFP fluorescence to detect micrometastasis. This finding suggests that this GFP-based approach has higher sensitivity for detecting occult lymph node metastasis as compared with standard histopathological examination. Thus, the two GFP-positive nodes, in which tumor cells were not detected histologically, could have contained microscopic metastasis that would have been identified by further sectioning. Other possible explanations of false-positive detection include either that GFP protein itself was produced in the primary tumor spread into regional lymph nodes or that high doses of OBP-401 entered nodes and incidentally replicated in normal lymphocytes in that they have low telomerase activity[24].

Although the molecular imaging strategy using OBP-401 is considered promising, some limitations of the system exist, the main one being the relatively short wavelength of excitation light of GFP. In contrast to luciferase, which is also commonly used for molecular imaging[25], if objects are located in the deep layer or covered with thick adjacent tissues, the excitation light for GFP may not be able to reach them. For example, when tumor foci were exposed to the surface of nodes opposite the illuminated field, GFP fluorescence could not be detected, thereby leading to false-negative detection. The extension of exposure time to the illumination allows increasing the fluorescence intensity; the excitation light, however, cannot penetrate deeper. To raise the imaging sensitivity, one possible approach is to make the specimen thinner, for example, by pressing the excised lymph nodes flat; the architecture of the nodes, however, may be destroyed. Alternatively, it might be useful to develop a hand-held probe, in which the outlet of the excitation beam light and the sensor of GFP fluorescence are combined. During surgery, metastatic lymph nodes could be positively identified with GFP fluorescence guided by this probe like a gamma probe for SLN biopsy. At least, a hand-held flashlight to excite GFP fluorescence has been reported[26].

Administration of OBP-401 can provide an additional advantage in cancer therapy. OBP-401, similar to OBP-301, is an oncolytic virus and selectively kills human tumor cells by viral replication; the process of cell death by OBP-401, however, is relatively slow in comparison with apoptosis-inducing chemotherapeutic drugs, because the virus needs time for replication. Therefore, tumor cells infected with OBP-401 express GFP fluorescence and then lose viability, allowing the timing of detection. We could speculate that OBP-401 would spread into the regional lymph nodes after intratumoral injection, express GFP signals in tumor cells by virus replication and finally kill tumor cells even if the surgeon failed to remove all nodes containing micrometastasis. Thus, the oncolytic activity of OBP-401 may function as a backup safety antitumor program.

In conclusion, we have demonstrated that the GFP-expressing telomerase-specific replication-selective adenovirus OBP-401 can be delivered into human tumor cells in regional lymph nodes and replicate with selective GFP fluorescence after injection into the primary tumor in an orthotopic rectal tumor model. The feasibility of original OBP-301 (Telomelysin) for human cancer therapy will be confirmed in clinical trials in the near future. Because the safety profiles of these two viruses are considered homologous, this molecular imaging strategy using OBP-401 has a potential of being widely available in humans as a navigation system in the surgical treatment of malignancy.

METHODS

Cell culture. The human non-small-cell lung cancer cell lines H1299 and H460, the human gastric cancer cell lines MKN28 and MKN45, the human colorectal cancer cell lines SW620 and HT29, the human esophageal cancer cell lines TE8 and T.Tn, the human prostate cancer cell lines LNCaP and PC-3, the human tongue squamous carcinoma cell lines HSC-3, HSC-4, SCC-4 and SCC-9, the human cervical adenocarcinoma cell line HeLa, the human hepatocellular carcinoma cell line HepG2, the human pancreatic cancer cell line Panc-1, the human mammary gland adenocarcinoma cell line MCF-7, the human osteosarcoma cell line U-2OS (ATCC), the NHLF cell line, the normal human renal epithelial cell line HRE, the human umbilical vascular endothelial cell line HUVEC (TaKaRa Biomedicals) and the normal human lung diploid fibroblast cell line WI38 (HSRRB) were cultured according to the vendor's specifications.

OBP-401. OBP-401 is a telomerase-specific replication-competent adenovirus variant in which the hTERT promoter element drives the expression of *E1A* and *E1B* genes linked with an internal ribosome entry site, with the *GFP* gene inserted under the CMV promoter into the E3 region for monitoring viral replication[27,28]. The virus was purified by ultracentrifugation in cesium chloride step gradients, their titers were determined by a plaque-forming assay using 293 cells and they were stored at –80 °C.

Quantitative real-time PCR analysis. Total RNA from the cultured cells was obtained using the RNeasy Mini Kit (QIAGEN). The *hTERT* mRNA copy number was determined by real-time quantitative RT-PCR using a LightCycler instrument and a LightCycler DNA TeloTAGGG Kit (Roche Molecular Biochemicals). DNA was extracted with the QIAamp DNA Mini Kit (QIAGEN), and quantitative real-time PCR assay for the *E1A* gene was also performed. The sequences of specific primers used for *E1A* were, sense: 5′-CCTGTGTCTAGAGAATGCAA-3′; antisense: 5′-ACAGCTCAAGTCCAAAG GTT-3′. PCR amplification began with a 600-s denaturation step at 95 °C and then 40 cycles of denaturation at 95 °C for 10 s, annealing at 58 °C for 15 s and extension at 72 °C for 8 s. Data analysis was performed using LightCycler Software (Roche Molecular Biochemicals). The ratios normalized by dividing the value of untreated cells were presented for each sample.

Fluorescence microscopy. Human cancer cell lines (H1299, SW620 and HT29) and normal cells (NHLFs) were infected with either 1 or 10 MOI of OBP-401 for 2 h *in vitro*. Expression of the *GFP* gene was assessed and photographed (magnification: ×200) using an Eclipse TS-100 fluorescent microscope (Nikon).

Electron microscopy. Human prostate cancer cell line LNCaP was infected with 10 MOI of OBP-401. Thin sections were cut on coated copper grids and stained with uranyl acetate. The samples were examined and photographed with a Hitachi H-7100 transmission electron microscope.

Immunohistochemistry. Immunohistochemical staining was performed using a Histofine SAB PO kit (Nichirei) according to the manufacturer's instructions. Paired tissues of primary tumors and lymph node metastases were obtained from gastric cancer patients who underwent surgery at Okayama University Hospital. Informed consent was obtained from each individual as approved by the Ethics Review Committee for Clinical Investigation of our institution. Formalin-fixed, paraffin-embedded tissue sections were mounted on silanized slides and deparaffinized. After blocking of nonspecific reactivity with rabbit or goat serum for 10 min at 25 °C, sections were incubated overnight at 4 °C with the monoclonal antibody to hTERT (Kyowa Medex). After rinsing, the slides were incubated with biotinylated rabbit antibody to mouse, and then with avidin-biotin-peroxidase complex. Peroxidase activity was determined using DAB-H_2O_2 solution (Histofine DAB substrate kit; Nichirei). The slides were counterstained with methyl green and Mayer's hematoxylin.

Animal experiments. The experimental protocol was approved by the Ethics Review Committee for Animal Experimentation of our institution. We

produced SW620 and HT29 xenografts on the back in 5-week-old female BALB/c *nu/nu* mice by subcutaneous injection of 5×10^6 SW620 or HT29 cells in 100 μl of HBSS using a 27-gauge needle. When tumors grew to ~6–7 mm in diameter, both tumors were intratumorally injected with OBP-401 (1×10^7 PFU/100 μl). Mice were anesthetized by intraperitoneal injection of pentobarbital (50 mg/kg) and examined for GFP expression. Six mice were used for each tumor cell line. To generate an orthotopic rectal cancer model, female BALB/c *nu/nu* mice were anesthetized and then placed in a supine position. The anorectal wall was cut at a length of 7 mm to prevent colonic obstruction resulting from rectal tumor progression. We injected cell suspension of HT29 cells at a density of 5×10^6 cells in 100 μl of Matrigel basement membrane matrix (Becton Dickinson Labware) slowly into the submucosal layer of the rectum through a 27-gauge needle (**Fig. 4a**). Four weeks later we injected 1×10^8 PFU/100 μl of OBP-401 directly into the rectal tumors. Mice were killed, and their abdominal spaces were examined at laparotomy 5 d after virus injection.

Cooled CCD imaging. *In vivo* GFP fluorescence imaging was acquired by illuminating the animal with a xenon 150-W lamp. The re-emitted fluorescence was collected through a long-pass filter on a Hamamatsu C5810 3-chip color CCD camera (Hamamatsu Photonics Systems). High-resolution images were acquired using an EPSON PC. Images were processed for contrast and brightness with the use of Adobe Photoshop 4.0.1J software (Adobe).

Note: Supplementary information is available on the Nature Medicine website.

ACKNOWLEDGMENTS

This work was supported in part by grants from the Ministry of Education, Culture, Sports, Science, and Technology of Japan (T.F. and S.K.); and by grants from the Ministry of Health, Labour, and Welfare of Japan (T.F.). We thank K. Nagai and H. Kawamura for the helpful discussion, and Y. Shirakiya and N. Mukai for the excellent technical support.

AUTHOR CONTRIBUTIONS

T.F. conceived the idea for this project, designed all experiments and wrote the manuscript. H.K., Y.W. and Y.H. performed all laboratory experiments and H.K., T.K. and Y.W. performed all animal experiments. S.K. provided crucial ideas and helped with data interpretation. T.F., F.U., F.T. and N.T. provided technical assistance. S.K. provided the hTERT promoter. H.M. constructed the OBP-401 virus. Y.U. developed a protocol for virus manufacture and validation.

COMPETING INTERESTS STATEMENT

The authors declare competing financial interests (see the *Nature Medicine* website for details).

Published online at http://www.nature.com/naturemedicine/
Reprints and permissions information is available online at http://npg.nature.com/reprintsandpermissions/

1. Tearney, G.J. *et al. In vivo* endoscopic optical biopsy with optical coherence tomography. *Science* **276**, 2037–2039 (1997).
2. MacDonald, S.L. & Hansell, D.M. Staging of non-small cell lung cancer: imaging of intrathoracic disease. *Eur. J. Radiol.* **45**, 18–30 (2003).
3. Kelloff, G.J. *et al.* Progress and promise of FDG-PET imaging for cancer patient management and oncologic drug development. *Clin. Cancer Res.* **11**, 2785–2808 (2005).
4. McMasters, K.M. *et al.* Sentinel lymph node biopsy for melanoma: controversy despite widespread agreement. *J. Clin. Oncol.* **19**, 2851–2855 (2001).
5. Kuerer, H.M. & Newman, L.A. Lymphatic mapping and sentinel lymph node biopsy for breast cancer: developments and resolving controversies. *J. Clin. Oncol.* **23**, 1698–1705 (2005).
6. Koopal, S.A. *et al.* Frozen section analysis of sentinel lymph nodes in melanoma patients. *Cancer* **89**, 1720–1725 (2000).
7. Tanis, P.J. *et al.* Frozen section investigation of the sentinel node in malignant melanoma and breast cancer. *Ann. Surg. Oncol.* **8**, 222–226 (2001).
8. Gulec, S.A., Su, J., O'Leary, J.P. & Stolier, A. Clinical utility of frozen section in sentinel node biopsy in breast cancer. *Am. Surg.* **67**, 529–532 (2001).
9. Chao, C. *et al.* Utility of intraoperative frozen section analysis of sentinel lymph nodes in breast cancer. *Am. J. Surg.* **182**, 609–615 (2001).
10. Misteli, T. & Spector, D.L. Applications of the green fluorescent protein in cell biology and biotechnology. *Nat. Biotechnol.* **15**, 961–964 (1997).
11. van Roessel, P. & Brand, A.H. Imaging into the future: visualizing gene expression and protein interactions with fluorescent proteins. *Nat. Cell Biol.* **4**, E15–E20 (2002).
12. Ehrhardt, D. GFP technology for live cell imaging. *Curr. Opin. Plant Biol.* **6**, 622–628 (2003).
13. Yang, M., Baranov, E., Moossa, A.R., Penman, S. & Hoffman, R.M. Visualizing gene expression by whole-body fluorescence imaging. *Proc. Natl Acad. Sci. USA* **97**, 12278–12282 (2000).
14. Hasegawa, S. *et al. In vivo* tumor delivery of the green fluorescent protein gene to report future occurrence of metastasis. *Cancer Gene Ther.* **7**, 1336–1340 (2000).
15. Ohtani, S. *et al.* Quantitative analysis of p53-targeted gene expression and visualization of p53 transcriptional activity following intratumoral administration of adenoviral p53 *in vivo*. *Mol. Cancer Ther.* **3**, 93–100 (2004).
16. Kawashima, T. *et al.* Telomerase-specific replication-selective virotherapy for human cancer. *Clin. Cancer Res.* **10**, 285–292 (2004).
17. Taki, M. *et al.* Enhanced oncolysis by a tropism-modified telomerase-specific replication selective adenoviral agent OBP-405 ("Telomelysin-RGD"). *Oncogene* **24**, 3130–3140 (2005).
18. Umeoka, T. *et al.* Visualization of intrathoracically disseminated solid tumors in mice with optical imaging by telomerase-specific amplification of transferred green fluorescent protein gene. *Cancer Res.* **64**, 6259–6265 (2004).
19. Gu, J., Andreeff, M., Roth, J.A. & Fang, B. hTERT promoter induces tumor-specific Bax gene expression and cell killing in syngenic mouse tumor model and prevents systemic toxicity. *Gene Ther.* **9**, 30–37 (2002).
20. Tsutsumi, S., Kuwano, H., Morinaga, N., Shimura, T. & Asao, T. Animal model of paraaortic lymph node metastasis. *Cancer Lett.* **169**, 77–85 (2001).
21. Maehara, Y. *et al.* Clinical significance of occult micrometastasis in lymph nodes from patients with early gastric cancer who died of recurrence. *Surgery* **119**, 397–402 (1996).
22. Coello, M.C., Luketich, J.D., Litle, V.R. & Godfrey, T.E. Prognostic significance of micrometastasis in non-small-cell lung cancer. *Clin. Lung Cancer* **5**, 214–225 (2004).
23. Fujiwara, T. *et al.* Multicenter phase I study of repeated intratumoral delivery of adenoviral p53 (ADVEXIN) in patients with advanced non-small cell lung cancer. *J. Clin. Oncol.* **24**, 1689–1699 (2006).
24. Hiyama, K. *et al.* Activation of telomerase in human lymphocytes and hematopoietic progenitor cells. *J. Immunol.* **155**, 3711–3715 (1995).
25. Adams, J.Y. *et al.* Visualization of advanced human prostate cancer lesions in living mice by a targeted gene transfer vector and optical imaging. *Nat. Med.* **8**, 891–897 (2002).
26. Yang, M., Luiken, G., Baranov, E. & Hoffman, R.M. Facile whole-body imaging of internal fluorescent tumors in mice with an LED flashlight. *Biotechniques* **39**, 170–172 (2005).
27. Watanabe, T. *et al.* Histone deacetylase inhibitor FR901228 enhances the antitumor effect of telomerase-specific replication-selective adenoviral agent OBP-301 in human lung cancer cells. *Exp. Cell Res.* **312**, 256–265 (2006).
28. Fujiwara, T. *et al.* Enhanced antitumor efficacy of telomerase-selective oncolytic adenoviral agent OBP-401 with docetaxel: preclinical evaluation of chemovirotherapy. *Int. J. Cancer* **119**, 432–440 (2006).